

A 600 ks *Chandra* View of Abell 2597: Multiple Epochs of AGN Activity, Shocks, and a Plasma Depletion Layer

OSASE OMORUYI ,¹ GRANT TREMBLAY ,¹ ALEXEY VIKHLININ ,¹ PRATIK DABHADE ,² SOMAK RAYCHAUDHURY ,³ MAXIM MARKEVITCH ,⁴ JOHN ZUHONE ,¹ PAUL NULSEN ,¹ STEFI A. BAUM ,⁵ CHRISTOPHER P. O'DEA ,⁵ TRACY CLARKE ,⁶ SCOTT RANDALL ,¹ PREETI KHARB ,⁷ SANNA GULATI ,⁷ SRAVANI VADDI ,⁸ AND FRIENDS :)

¹Center for Astrophysics | Harvard & Smithsonian, 60 Garden St., Cambridge, MA 02138, USA

²Astrophysics Division, National Centre for Nuclear Research, Pasteura 7, 02-093 Warsaw, Poland

³Ashoka University, Dept. Of Physics, Sonipat, Haryana-131029, India

⁴NASA Goddard Space Flight Center, Code 662, Greenbelt, MD 20771

⁵University of Manitoba, Dept. of Physics and Astronomy, Winnipeg, MB R3T 2N2, Canada

⁶U.S. Naval Research Laboratory, 4555 Overlook Avenue SW, Washington, DC 20375, USA

⁷National Centre for Radio Astrophysics, Tata Institute for Fundamental Research, Savitribai Phule Pune University, Ganeshkhind, Pune 411007, India

⁸Arecibo Observatory, NAIC, HC3 Box 53995, Arecibo, Puerto Rico, PR 00612, USA

ABSTRACT

We present deep (600 ks) *Chandra* X-ray observations of the cool-core galaxy cluster Abell 2597, providing the most detailed view of AGN-driven feedback and its effects on the hot intracluster medium in the cluster to date. We identify two new X-ray cavities, increasing the total number of detected cavities in the cluster to six, and three potential shock fronts located at radii of 50 kpc, 80 kpc, and 100 kpc, with Mach numbers ranging from 1.14 to 1.29. Additionally, we detect an elongated X-ray surface brightness channel aligned with the northern radio jet, likely corresponding to a plasma depletion layer caused by magnetic field draping. The sequence of cavity ages and shock fronts suggests a series of AGN outbursts over the past 100 Myr. Despite the substantial energy input from these cavities and shocks ($\sim 1 \times 10^{44}$ ergs s⁻¹), they do not fully offset radiative cooling ($L_{\text{cool}} \sim 1 \times 10^{44}$ ergs s⁻¹), as indicated by the presence of a $\sim 10^9 M_{\odot}$ cold gas reservoir spatially coincident with the hot X-ray gas. To better understand how the AGN is fueled, we compared the observed cavity power to the estimated Bondi accretion rate, finding that hot mode accretion—where the supermassive black hole accretes directly from the surrounding hot gas—is insufficient to sustain the AGN activity. Instead, we find further evidence supporting cold mode accretion, where thermally unstable gas condenses into dense clouds that fall toward the black hole, with observed signatures of infalling cold clouds near the supermassive black hole.

Keywords: galaxies: clusters: individual: Abell 2597 - X-rays: galaxies: clusters.

1. INTRODUCTION

Galaxy clusters, the largest gravitationally bound structures in the Universe, consist of hundreds to thousands of galaxies embedded in a vast expanse of diffuse plasma known as the intracluster medium (ICM). While the ICM is generally characterized by its hot ($\sim 10^7$ – 10^8 K) and diffuse nature, approximately half of all galaxy clusters exhibit a distinct feature known as a “cool core.” In these clusters, the central region contains a significant overdensity of rapidly cooling, X-ray bright plasma. As this hot plasma cools, it loses pressure support, resulting in a continuous inflow of cooler, multiphase gas

toward the central brightest cluster galaxy (BCG). According to the classical “cooling flow” model, this process should fuel star formation rates of up to several hundred solar masses per year near the cluster’s core. However, observations consistently fail to detect such extreme star formation rates, suggesting that either the remaining cooling is hidden from view (e.g., Fabian et al. 2022a, 2023), and/or some mechanism, most likely mechanical feedback from the BCG’s central supermassive black hole, must be counteracting the cooling flow (for comprehensive reviews, see Veilleux et al. (2005); McNamara & Nulsen (2007); Alexander & Hickox (2012);

Fabian (2012); McNamara & Nulsen (2012); Gaspari et al. (2013); Kormendy & Ho (2013)).

Abell 2597 ($z = 0.0821$), a nearby cool core cluster of galaxies, serves as a canonical observational example of how AGN feedback regulates the cooling process in cluster cores, which in turn accounts for the lack of extreme star formation in central galaxies and explains the steep decline in the galaxy luminosity function at high luminosities (Bower et al. 2006; Croton et al. 2006). Within the rapidly cooling hot atmosphere of Abell 2597, the BCG’s central supermassive black hole expels powerful radio jets, establishing a ~ 30 kpc network of buoyantly rising bubbles observed as X-ray ‘cavities’ (Tremblay et al. 2012a). As the bubbles rise buoyantly and expand, they heat the surrounding X-ray plasma and offset radiative losses from the ICM (Churazov et al. 2002; Tremblay et al. 2012a). This “feedback” slows the cooling flow, reducing the classical cooling flow rate from $\sim 500M_{\odot}\text{yr}^{-1}$ to a residual $\sim 20 - 75M_{\odot}\text{yr}^{-1}$, as indicated by O VI ultraviolet emission tracing gas cooling at $\sim 7 \times 10^5$ K (Oegerle et al. 2001), and consistent with a recent estimate of $\sim 67 M_{\odot}\text{yr}^{-1}$ based on hidden X-ray-emitting cooling flows obscured by cold clouds and dust (Fabian et al. 2023). In addition to mitigating intracluster gas cooling, the bubbles have likely uplifted the observed multiphase filamentary nebula that spans the inner ~ 30 kpc of the galaxy Tremblay et al. (2012b, 2018).

Recent ALMA CO(2-1) observations of the cold, star-forming gas near the heart of the BCG revealed three deep absorption lines, redshifted by $+300$ km s $^{-1}$ against the mm-synchrotron continuum source associated with the black hole (Tremblay et al. 2016, 2018). These absorption features are potential “shadows” cast by infalling cold molecular clouds, supplying a large (~ 0.1 to a few $M_{\odot}\text{ yr}^{-1}$) mass flux of cold molecular gas towards the black hole accretion reservoir. This inflowing cold gas will eventually be accreted and fuel another powerful AGN response, continuing a cycle where the black hole acts as the “pump” of a galaxy-spanning “fountain.” In this galactic fountain, cold gas clouds drain into the black hole accretion reservoir, powering jets and bubbles that uplift a cooling plume of low-entropy multiphase gas, which may stimulate additional cooling and accretion as part of a self-regulating feedback loop (Tremblay et al. 2018).

To map the hot phase of A2597’s billion solar mass cold molecular fountain, Tremblay et al. (2012a) published ~ 120 ks of *Chandra* data, revealing a highly anisotropic surface brightness distribution in the clus-

ter, with an inner 30 kpc network of X-ray cavities more extensive than previously documented. The largest of these cavities, ~ 25 kpc in projected length, is co-spatial with extended 330-MHz radio emission. Additionally, a ~ 15 -kpc soft excess X-ray filament was identified, aligned with the cavity and radio axis, and partially co-spatial with a hook-like extension of 1.3-GHz radio emission. The X-ray filament may be associated with the dredge-up of multiphase gas, ranging in temperature from 10^3 to 10^7 K, by the propagating radio source, making it a potential example of a dramatic interaction between the radio jets and the surrounding gas. However, the limited depth of the X-ray and radio data did not allow these features to be fully resolved, preventing a comprehensive understanding of the AGN feedback processes at play.

Deep X-ray observations with the *Chandra* X-ray Observatory, often spanning hundreds of kiloseconds and, in rare cases, megaseconds of exposure time, have been instrumental in examining the imprints AGN feedback leaves on the hot ICM. These long exposures have enabled the detection of faint features and subtle variations in the ICM, resulting in the discovery of multiple generations of AGN feedback-driven cavities (e.g., Perseus, NGC 5813 Fabian et al. 2003; Randall et al. 2015), weak shock fronts surrounding powerful AGN outbursts (e.g., Hydra A, Cygnus A, MS 0735.6+7421, Abell 2052, Hercules A Nulsen et al. (2005); Snios et al. (2018); Liu et al. (2019); Ubertosi et al. submitted), and in extreme cases, ripples—interpreted as multiple weak shock fronts—propagating outward into the large-scale ICM (e.g., Perseus Fabian et al. 2006). Building on this legacy of deep *Chandra* observations, this paper presents an additional 480 ks of data for Abell 2597, resulting in a total exposure time of 590 ks. To complement this deep X-ray dataset and gain a comprehensive understanding of the AGN feedback history in Abell 2597, we also tangentially present archival low-frequency radio observations from the Giant Metre Radio Telescope (GMRT), UV observations from the *Hubble Space Telescope*’s Cosmic Origins Spectrograph (HST COS), and near-infrared integral field unit observations from the Spectrograph for INtegral Field Observations in the Near Infrared (SINFONI).

This paper is structured as follows: In Section 2, we describe the deep X-ray data as well as archival radio, ultraviolet, and near-infrared data presented in this work in Section 2. Section 3 presents a comprehensive description of both newly identified and previously reported features in the intracluster medium (ICM), such as the extended network of cavities, large-scale cocoon shocks, and an X-ray channel. In this section, we also present

Table 1. SUMMARY OF ABELL 2597 OBSERVATIONS

Waveband/Line (1)	Facility (2)	Instrument/Config. (3)	Exp. Time (4)	Prog./Obs.ID (Date) (5)	Reference (6)
X-ray (0.2 - 10 keV)	<i>Chandra</i>	ACIS-S/VFAINT	52.20 ks	6934 (2006 May 1)	Tremblay et al. (2012a, 2012b)
...	60.11 ks	7329 (2006 May 4)	Tremblay et al. (2012a, 2012b)
...	69.39 ks	19596 (2017 Oct 8)	(Large Program 18800649)
...	44.52 ks	19597 (2017 Oct 16)	...
...	14.34 ks	19598 (2017 Aug 15)	...
...	24.73 ks	20626 (2017 Aug 15)	...
...	20.85 ks	20627 (2017 Aug 17)	...
...	10.92 ks	20628 (2017 Aug 19)	...
...	56.36 ks	20629 (2017 Oct 3)	...
...	53.4 ks	20805 (2017 Oct 5)	...
...	37.62 ks	20806 (2017 Oct 7)	...
...	79.85 ks	20811 (2017 Oct 21)	...
...	62.29 ks	20817 (2017 Oct 19)	...
<i>K</i> -band	VLT	SINFONI + AO	3600 s	093.B-0638(C) (2014 Jul 19)	this paper
FUV	HST	COS G140L	13952.640 s	30-Oct 2014	Vaddi et al (in prep)
Radio	GMRT	Band 3	85 mins	05DAG01 (20-Mar 2004)	this paper
...	...	Band 4	1969 mins	19_010 (20-Dec 2010)	this paper

NOTE—Summary of all new and archival observations of Abell 2597 presented in this paper. The observations are presented in descending order of wavelength, from X-ray through radio. (1) Waveband or Line Name targeted by the observation; (2) telescope used; (3) instrument (and aperture/detector) used for observation; (4) on-source exposure time; (5) date of observation; (6) reference to publication(s) where the listed data first appeared or were otherwise discussed in detail.

detailed thermodynamic profiles of the ICM, and analyze X-ray and radio signatures of the cavities, channel and potential expanding cocoon. In Sections 4 and 5, we examine the heating and cooling balance within the cluster and the potential origin of the x-ray channel. Throughout this paper, we assume $H_0 = 70 \text{ km s}^{-1} \text{ Mpc}^{-1}$, $\Omega_M = 0.27$, and $\Omega_\Lambda = 0.73$. In this cosmology, $1''$ corresponds to 1.549 kpc at the redshift of the BCG, where the associated angular size and luminosity distances are 319.4 and 374.0 Mpc, respectively, and the age of the Universe is 12.78 Gyr. Unless otherwise noted, all images are centered on the nucleus of the A2597 BCG at right ascension (R.A.) 23h 25m 19.7s and declination -12° 07'27" (J2000), with east left and north up.

2. OBSERVATIONS AND DATA REDUCTION

We summarize all new and archival observations of Abell 2597 presented in this paper in Table 1. A comprehensive description of the analysis methods applied for each dataset is provided in Appendix A. To ensure transparency and facilitate reproducibility, all Python codes/Jupyter Notebooks used and created to analyze the data are publicly available in an online repository.¹

2.1. *Chandra* X-ray Observations

As part of Cycle 18 program 18800649 (PI: Tremblay), the *Chandra* X-ray Observatory observed Abell 2597 for a total of 474.3 ks in August and October 2014 (ObsIDs 19596, 19597, 19598, 20626, 20627, 20628, 20629, 20805, 20806, 20811, and 20817). We also included 112.3 ks from the two older, previously published observations (ObsIDs 6934 and 7329, PI: Clarke; McNamara et al. 2001; Clarke et al. 2005; Tremblay et al. 2012a,b) in our analysis. Combined, these observations provide a total integration time of 586.6 ks across fourteen separate ACIS-S observations.

All ObsIDs were processed using the latest versions of CIAO v4.16 (*Chandra* Interactive Analysis of Observations; Fruscione et al. 2006) and CALDB v4.11.5. We reprocessed the data with *chandra_repro* and identified and filtered flares using the ChIPS routine LC_CLEAN. No significant flares were detected in the Cycle 18 data, requiring no time to be rejected. Point sources were identified through a wavelet decomposition technique (Vikhlinin et al. 1998) and visually inspected before masking. It is important to note that although A2597 remains a constant source of X-rays, the optical blocking filter on ACIS degrades over time, leading to significant contaminant buildup. As a result, the early *Chandra* observations have count rates nearly twice as high as those obtained a decade later, which explains why, despite having nearly half the observing time of the nearby Perseus cluster—where 890 ks of data yielded almost 70

¹ <https://github.com/osaseo/chandraA2597>

million counts (Fabian et al. 2006)—the nearly 600 ks of observations for Abell 2597 have yielded only 1.5 million counts within a $\sim 130''$ radius.

2.2. Archival GMRT Radio Observations

The GMRT observed Abell 2597 multiple times over two decades (2000–2020) at a range of frequencies: 157 MHz (PI: Somak Raychaudhury), 244 MHz (PI: Tracy Clarke), 311 MHz (PI: Nithyanandan Thyagarajan), 610 MHz (PIs: Vasant Krishna Kulkarni, David Alan Green), 614 MHz (PI: Tracy Clarke), and 629 MHz (PI: Somak Raychaudhury). Unfortunately, most of the data were severely affected by radio frequency interference (RFI), rendering them unsuitable for producing spatially resolved views of the radio emission. The only datasets successfully recovered for analysis were the observations at 244 MHz (Band 3; PI: Raychaudhury) and 610 MHz (Band 4; PI: Green).

2.3. Archival SINFONI Observations

The nucleus of A2597 was targeted with the Spectrograph for INtegral Field Observations in the Near Infrared (SINFONI; Eisenhauer et al. (2003)) on the Very Large Telescope (VLT). Under ESO Program ID 093.B-0638(C) (PI: Raymond), the near-infrared (NIR) observations were performed in the K-band filter (1.95–2.45 μm), providing integral field data cubes covering the H_2 (ro)vibrational lines. The observations were performed using the Laser Guide Star (LGS) Adaptive Optics (AO) mode (Bonnet et al. 2003). Strap-length limits required that tip/tilt correction, which compensates for small-scale variations in the wavefront caused by atmospheric turbulence and improves spatial resolution, be attempted on the A2597 nucleus. The correction, however, was unsuccessful, for the nucleus lacked sufficient contrast against the blurred galaxy caused by atmospheric conditions. Consequently, the observations were conducted in a “seeing enhancer mode” which enables us to achieve a spatial resolution of 0''.6 (FWHM), only a moderate increase in spatial resolution relative to the previous 1'' seeing-limited images of the nucleus published in Oonk et al. (2010). The SINFONI-AO data reduction was performed using ESOREX (3.13.6) following the workflow 3.3.2 under the EsoReflex environment (Freudling et al. 2013).

3. THE DEEPEST VIEW OF THE HOT ICM

3.1. X-ray Morphology and Features

Figure 1 presents the new background-subtracted, exposure-corrected, 0.5–7.0 keV *Chandra* X-ray image of the Abell 2597. The top panel shows the central 550 kpc \times 340 kpc environment, with the image binned to 4

pixels to enhance the visibility of large-scale structures. The X-ray emission displays a centrally peaked morphology, characteristic of cool-core clusters, and gradually decreases in intensity toward the outskirts, transitioning into a more diffuse, extended halo. The emission is broadly anisotropic, with pronounced extensions toward the northeast and southwest.

The most prominent structures in the cluster are concentrated in its central region, highlighted in the lower panel of Figure 1, which focuses on the inner 180 kpc \times 110 kpc. The X-ray emission surrounding nuclear region with the central radio source is marked with a cross, forms a backward ‘S’ shape due to surface brightness deficits to the northeast and west. We identify each prominent surface brightness deficit using numerical labels. White numbers indicate regions previously identified in earlier X-ray studies of the cluster, while bold blue numbers represent new structures discovered in this work. A brief list of these structures is provided in Table 2. The spatial relationship between these X-ray structures and the 330 MHz, 1.3 GHz, and 8.4 GHz radio emission is illustrated in Figure 2.

The first *Chandra* X-ray study of Abell 2597 by McNamara et al. (2001) (hereafter M01), despite its relatively short 32 ks exposure, found two prominent cavities in the ICM, situated 18'' away from the X-ray surface brightness peak. One cavity resides to the northwest, and the other to the southeast. Their considerable distance from the central AGN led to their designation as “ghost” cavities, i.e. cavities associated with an older epoch of feedback from the AGN. Clarke et al. (2005) (hereafter C05) subsequently analyzed the same *Chandra* data by subtracting a smooth elliptical model from it to better highlight features in the ICM. The residual image revealed a distinct cavity to the northeast, as well as a potential ‘X-ray tunnel’ connecting the southwestern cavity with the central radio source. The nature of the latter feature, however, remained ambiguous, as it could either be a discrete structure or part of a larger cavity encompassing both the tunnel and the M01 cavity.

Deeper *Chandra* observations, with nearly four times the prior exposure time (120 ks), presented in Tremblay et al. (2012a,b) (hereafter T12a and T12b) discovered that the network of X-ray cavities was more spatially extended than previously thought. Notably, the western ghost cavity described by M01 and C05 (features 1 and 2) appeared to be part of a larger ‘teardrop’ shaped cavity ~ 25 kpc in projected length. While the precise morphology of this structure remained ambiguous, we retain the labeling of two distinct features for consistency with previous work and the spectral analysis

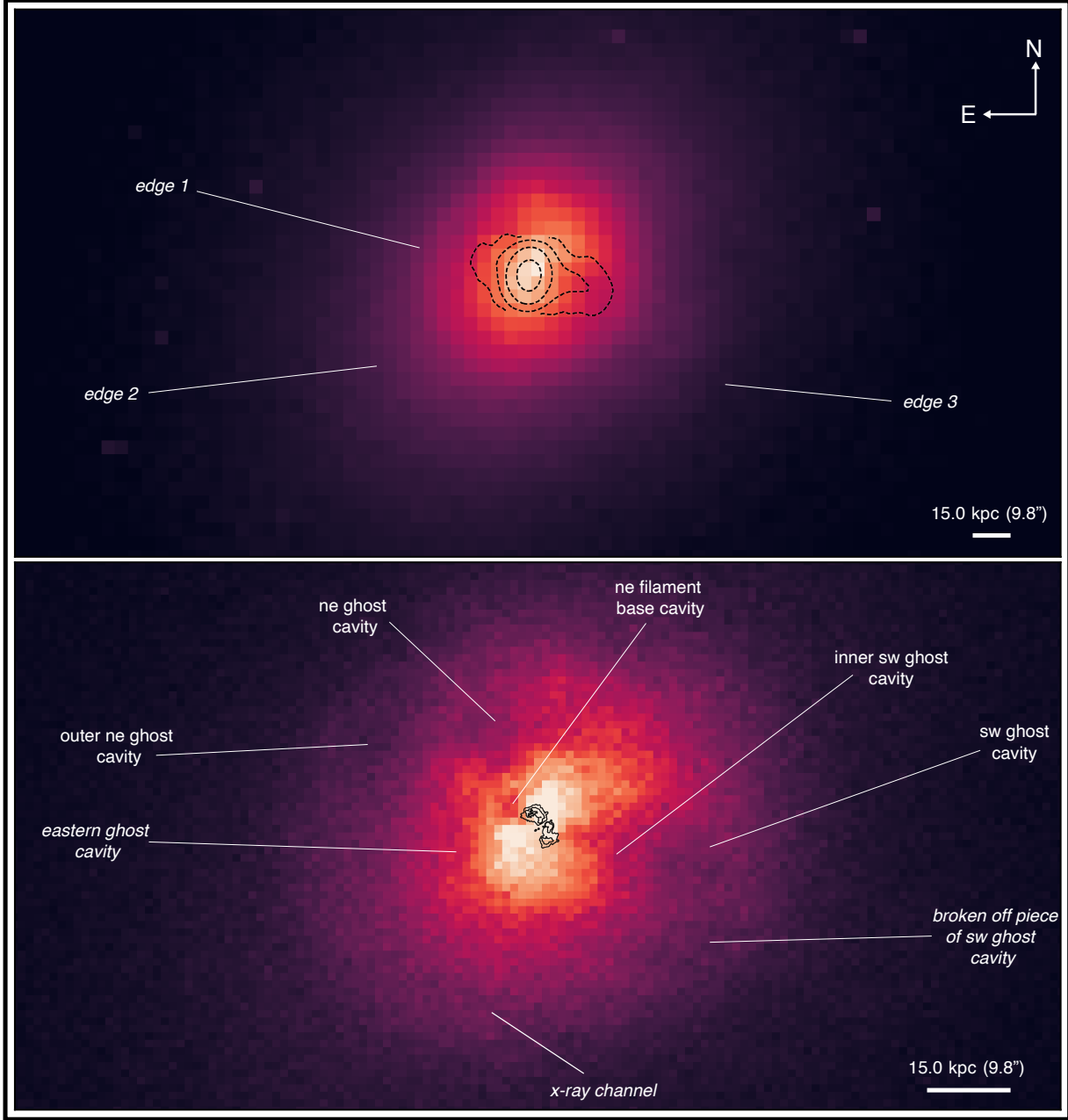


Figure 1. Raw, exposure-corrected 0.5–7 keV images of all merged *Chandra* observations (see Table 1). Newly detected features are italicized. The top panel shows the broader $\sim 550 \times 340$ kpc environment of Abell 2597, with the image binned by a factor of 8. 2–3 surface brightness edges are visible across each side of the anisotropic surface brightness distribution, resembling the edges of a “shocked cocoon.” The bottom panel zooms into the central $\sim 180 \times 110$ kpc region, with the image binned by a factor of 2. We identify seven cavities and a distinct X-ray channel.

presented below. Furthermore, T12b identified an additional northeastern ghost cavity.

Our new, additional 480 ks of clean data has once again revealed that each of the previously identified structures is more extensive than previously thought. Notably, the M01 ghost cavity, in addition to showing a connection to the C05 cavity, now shows an apparent connection with the surface brightness deficit located di-

rectly below it, resembling a potentially sheared piece of the M01 cavity. Additionally, we identify a potential new ghost cavity southeast of the surface brightness peak. This elliptical feature lies roughly opposite the teardrop-shaped cavity (the inner and outer southwestern ghost cavities). Whether it extends eastward remains uncertain, leaving open the possibility of a more elongated morphology akin to the teardrop cavity.

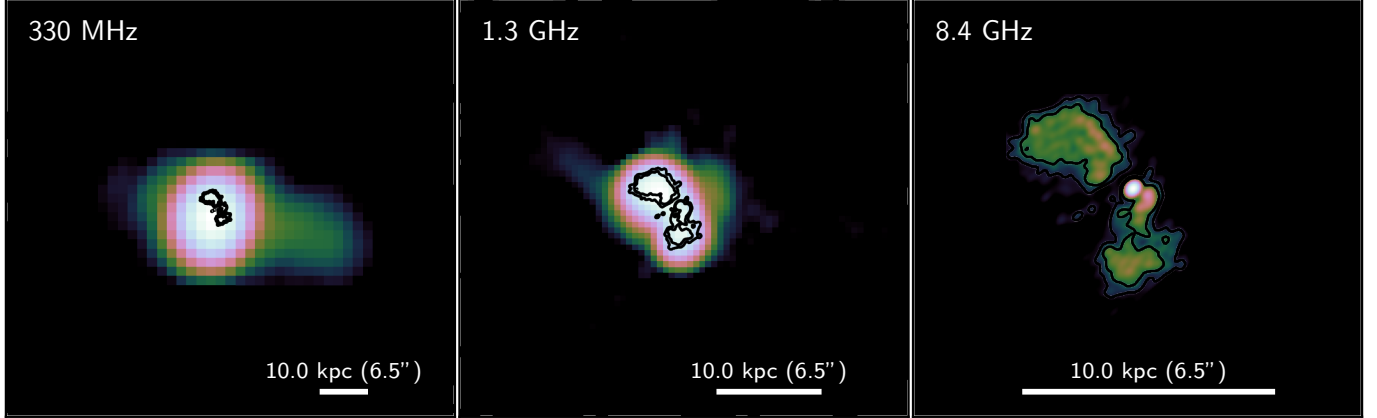


Figure 2. Archival 330 MHz, 1.3 GHz, and 8.4 GHz radio observations of Abell 2597. The top row displays the radio emission at each frequency, with 8.4 GHz radio contours overlaid for reference.

Lastly, we identify a thin, elongated surface brightness depression extending from the southern ICM. The feature curves upwards and inwards, connecting to the eastern and northeastern ghost cavities. Given its morphology, we tentatively classify it as an X-ray brightness “channel,” similar to structures observed in the atmospheres of Abell 520 and Abell 2142 (Wang et al. 2016; Wang & Markevitch 2018).

In the outer regions of the cluster’s atmosphere, we observe three subtle, nearly elliptical surface brightness edges around the cluster, highlighted by dashed white arcs. The most prominent edge is located just outside the primary central region, with a major axis of 37''.7 (57.7 kpc) and minor axis of 31''.5 (48.1 kpc). The second surface brightness edge is located further out, with a major axis of 55'' (84 kpc) and a minor axis of 50''.2 (76.6 kpc). The final edge is most prominent in the southwestern region of the anisotropic surface brightness distribution, with a major axis of 73''.2 (111.8 kpc) and a minor axis of 65''.8 (100.5 kpc). The first edge coincides with the extension of the low-frequency 330 MHz radio source, shown in the left panel of Figure 2.

These edges, if real, may represent signatures of expanding “cocoon” shells, created from the backflow of the ICM around the expanding bubbles inflated by radio AGN. Detecting such cocoons is notoriously difficult due to their faintness. Consequently, only a handful of studies have observed them in great detail, namely Hydra A (Nulsen et al. 2005), Cygnus A (Snios et al. 2018), and RBS 797 (Ubertosi et al. 2023). They have also been detected, though with less significance, in shallower *Chandra* observations of clusters such as MS 0735.6+7421 (Vantyghem et al. 2014) and 3C 88 (Liu et al. 2019). We further examine the nature of these potential AGN-driven cocoons in Section 3.4.

Table 2. Notable Features in Abell 2597’s ICM

Feature	Ref.
Edge 1	New
Edge 2	New
Edge 3	New
SW Ghost Cavity	M01
Inner SW Ghost Cavity	C05
NE Ghost Cavity	M01
Outer NE Ghost Cavity	T12(a,b)
NE Filament Base Cavity	C05
Eastern Ghost Cavity	New
Broken off Piece of SW Ghost Cavity	New
Channel	New

3.2. Thermodynamic Profiles

We present comprehensive thermodynamic profiles of the ICM in Figure 3. Key X-ray properties, including the total cluster mass M_Δ , radius R_Δ , central temperature kT_0 , central entropy K_0 , central pressure P_0 , and central cooling time $t_{\text{cool},0}$, are listed in Table 3.

The projected emission measure profile (Figure 3, left) confirms the central excess characteristic of cool-core clusters. The modified β -model from Vikhlinin et al. (2006) provides a good overall fit to the data, with $\chi^2 = 0.023$. However, several deviations from the model are evident within the grey shaded region marking the central 60 kpc radius, where multiple surface brightness depressions are associated with X-ray cavities.

At low redshift, cool-core clusters typically exhibit central cusps in their X-ray surface brightness distributions. Vikhlinin et al. (2007) characterized these cusps using the power-law index of the gas density profile, $\alpha = -2 d \log \rho_g / d \log r$, evaluated at $r = 0.04R_{500}$. Clusters hosting strong cool cores typically have $\alpha > 0.7$. While

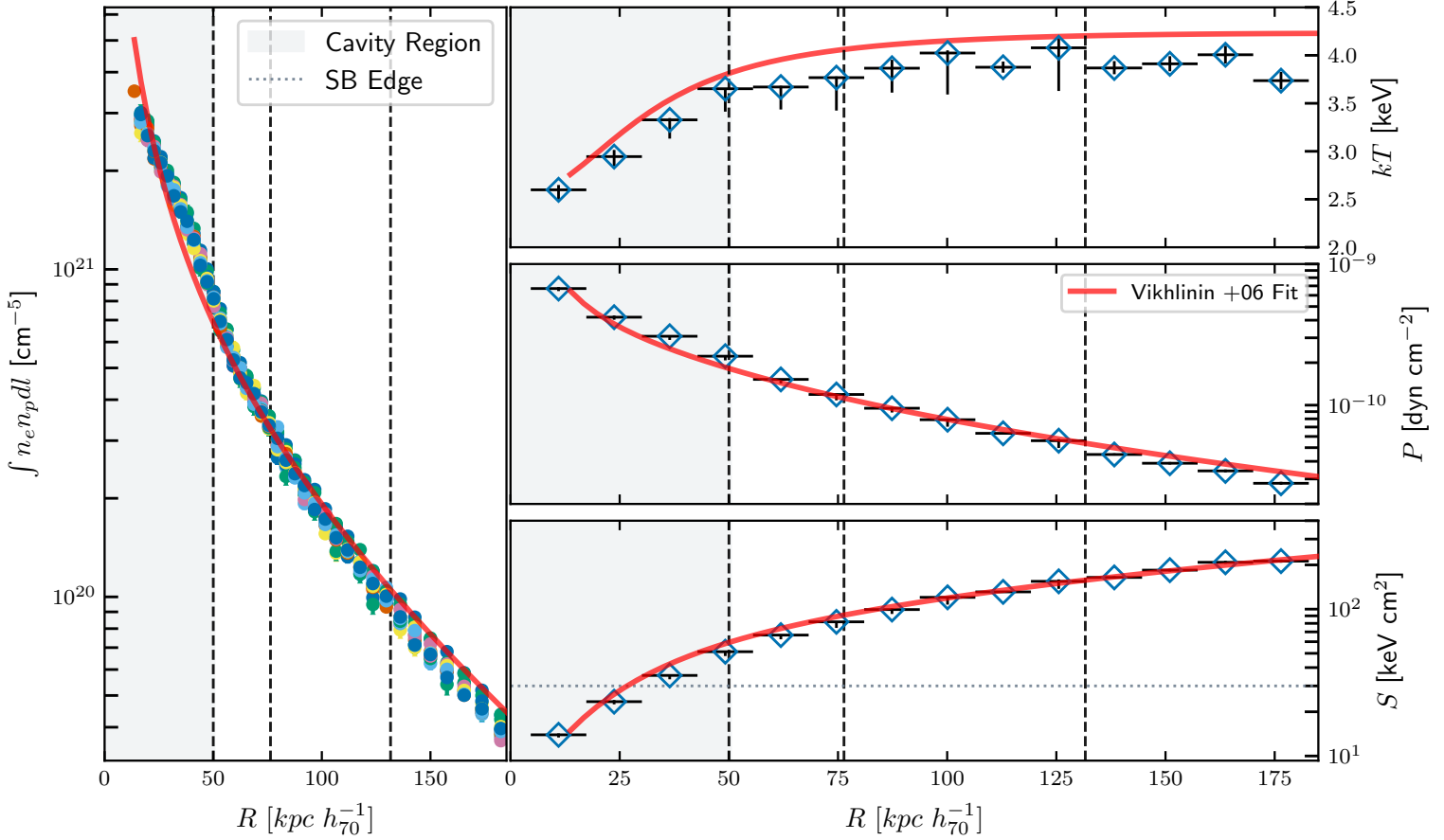


Figure 3. Spectral profiles fit with models from Vikhlinin et al. (2006) (V+06; red line). *Left:* X-ray emissivity per unit area for all *Chandra* ObsIDs (colorful points), fit with a modified beta model. *Top right:* Temperature profile using linearly spaced annuli (open diamonds), and the temperature model fit using log-spaced annuli. *Middle right, bottom:* Pressure and entropy profiles.

Table 3. X-RAY PROPERTIES

Property (units)	Value
$M_{500} - Y_X$ ($10^{14} M_\odot$)	2.28 ± 0.018
R_{500} (kpc)	904.8 ± 2.4
kT_0 (keV)	$2.938^{+0.028}_{-0.029}$
Z_0 (Z_\odot)	0.441 ± 0.019
K_0 (keV cm^2)	16.6 ± 0.07
P_0 (10^{-10} $dyn\ cm^{-2}$)	5.53 ± 0.024
$t_{cool, 0}$ (Gyr)	0.45 ± 0.004

NOTE—Summary of key X-ray properties of Abell 2597 at a radius of 12.5 kpc. M_{500} and R_{500} are calculated assuming hydrostatic equilibrium and the $Y_X - M$ relation from Vikhlinin et al. (2009). The central temperature kT_0 , abundance Z_0 , pressure P_0 , entropy K_0 , and cooling time $t_{cool, 0}$ are extracted from log-spaced annuli.

Vikhlinin et al. (2007) previously reported $\alpha = 1.1$ for A2597, our deeper data reveal a steeper value of $\alpha = 2.4$, further confirming the presence of a strong cool core.

The projected temperature profile (Figure 3, top left) shows a clear decline towards the center, dropping from 4.2 keV at $r \sim 120$ kpc to 2.75 keV in the core. This corresponds to a three-dimensional temperature drop

of $T_{min}/T_0 \sim 0.68$, consistent with other well-studied strong cool-core clusters.

The pressure profile (middle right panel) shows a steep decline with radius, mirroring the gradual decrease from the center outward. The entropy profile (bottom right panel) similarly follows the temperature profile, with lower entropy gas in the core, reaching a minimum of 15 keV cm^2 , well below the threshold of 30 keV cm^2 for star formation in cool cores (dashed horizontal line). Both profiles reveal local enhancements and decrements within the cavity-dominated region and the potential cocoon shock region, shaded in light red, which we thoroughly examine below in Sections 3.3 and 3.4.

3.3. The Central 65 kpc

3.3.1. Spectral Properties

Figure 4 presents the temperature distribution within the central 65 kpc of the cluster. In the left panel, the temperature map shows that the gas is coolest in the very center, as expected for cool core clusters. The coolest gas in the very center mirrors the backward 'S' shape of the central surface brightness region. The overall central cooling region is anisotropic, with extended

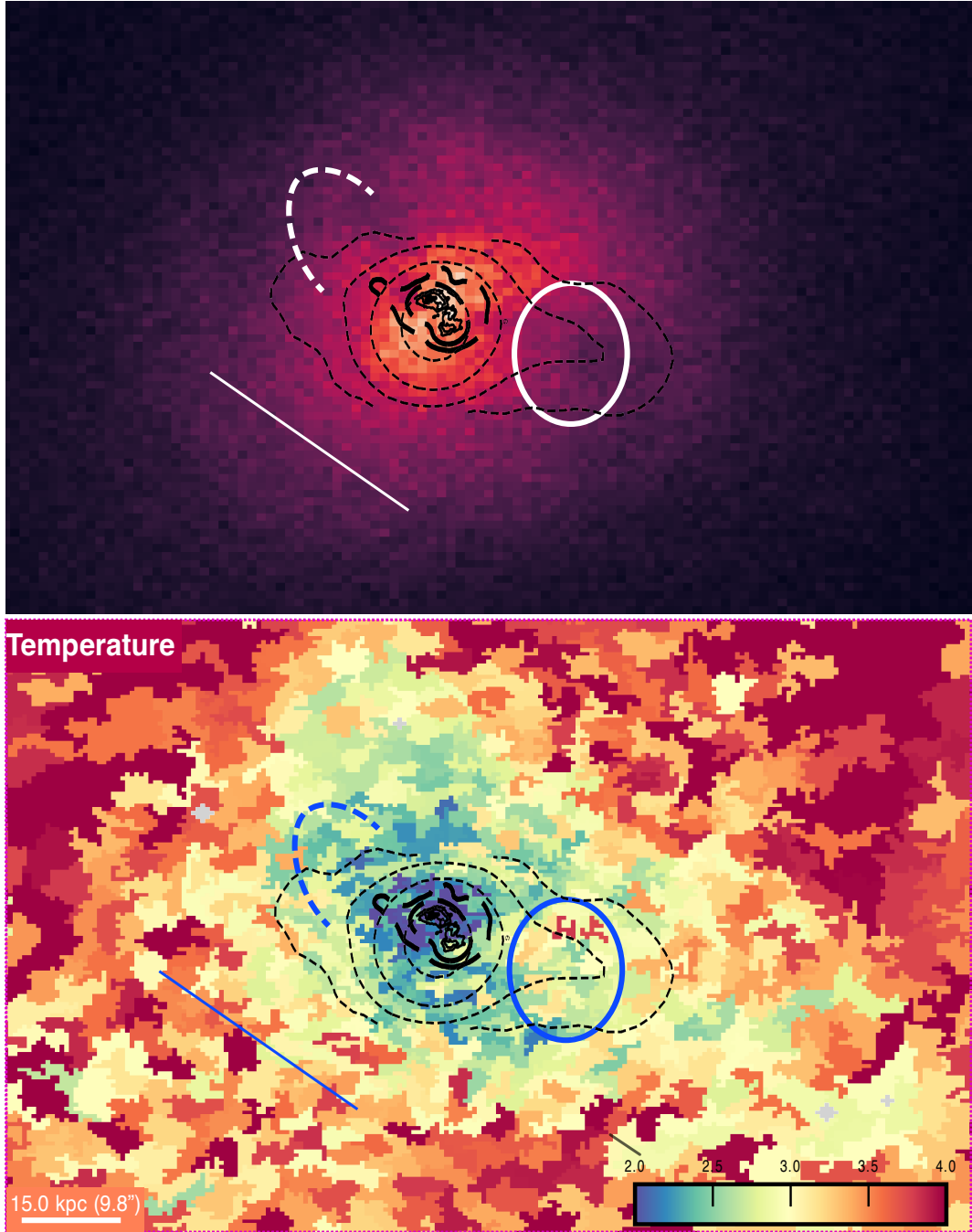


Figure 4. Top: *Chandra* X-ray image from Figure 1 with key spectral features overlaid. The solid white line marks the elongated X-ray surface brightness channel, dashed white arc indicates the ridge of cool gas co-spatial with the 1.3 GHz radio emission, and white circle highlights the location of the “hot arc.” Bottom: Temperature map of the ICM in Abell 2597, showing the same overlaid features.

cooling to the north along the axis of young 8.4 GHz radio source, and extended cooling to the east along the axis of the old 330 MHz radio source.

In the right panel, we show the same region, now with X-ray surface brightness contours overlaid. Within the northern extension of cool gas, we confirm the presence of the ~ 15 kpc soft X-ray/ “cold” filament previously identified by T12b, spatially aligned with the extended X-ray filament. We find that this cold filament ex-

tends further northeast than previously observed, with a length of ~ 18 kpc. We also identify an additional region of cold gas north of the ICM, situated between the northeastern and northwestern ghost cavities. This filament, 20 kpc in length, is parallel to the northern radio jet axis and spatially corresponds to a stream of X-ray excess extending outwards between the two ghost cavities. In contrast, the ghost cavities themselves are filled with slightly warmer gas.

The centers of the remaining cavities are almost always surrounded by higher temperature gas. The exception to this rule is the potential broken off piece of the southwestern ghost cavity, which we interpret as a detached piece of the M01 cavity. The gas within this cavity is cooler than the gas outside of it. Within the region of the 330 MHz radio source, T12a detected an arc of hot, high entropy gas separating the cavities within the teardrop-shaped structure at S/N ~ 30 .

In Figure 5, we present the pseudo-pressure, entropy and abundance maps of the same central 65 kpc of the cluster. The pseudo pressure map largely traces the surface brightness distribution, showing cavities as low-pressure regions bordered by higher-pressure gas. This is particularly prominent in the teardrop cavity, where the contrast in pressure is most striking. The entropy distribution mirrors that of the temperature map, highlighting potential sites of gas cooling. The cavities generally coincide with regions of high entropy, with lower entropy/cooler gas surrounding their rims. Notably, the location of the hot arc shows elevated pressure and entropy in both maps, reinforcing the observations made in T12a that suggest this region may be subject to shock heating or increased turbulence.

The abundance map shows that most of the identified cavities coincide with regions of enhanced abundance. A notable abundance increase is observed near the tip of the northern radio lobe, while the teardrop cavity exhibits elevated abundances, particularly along its rims. Inside the teardrop cavity, the region associated with the hot arc also shows abundance enhancement. In contrast, the potential broken-off piece of the southwestern ghost cavity does not display significant abundance elevation.

3.3.2. X-Ray Cavity Sizes

We quantify the spatial extent of each cavity using the unsharp-masked image presented in Figure ???. Although most of the cavities identified have circular 2D shapes, the eastern ghost cavity exhibits a more ellipsoidal shape. We report each cavity's spherical radius or elliptical radii, as appropriate, in Table ???, and discuss the potential origins of each cavity further in Section 4.2.

3.3.3. Cavity Ages

We estimate the age of each cavity using two independent methods: calculating the buoyant rise time and analyzing the lifetime of the radio synchrotron emission. The results are summarized in Table 2.

To calculate the buoyant rise time, we assume each cavity originated as a buoyant bubble injected near the peak of the X-ray emission, where the active radio source is currently located. The bubble then rose buoyantly

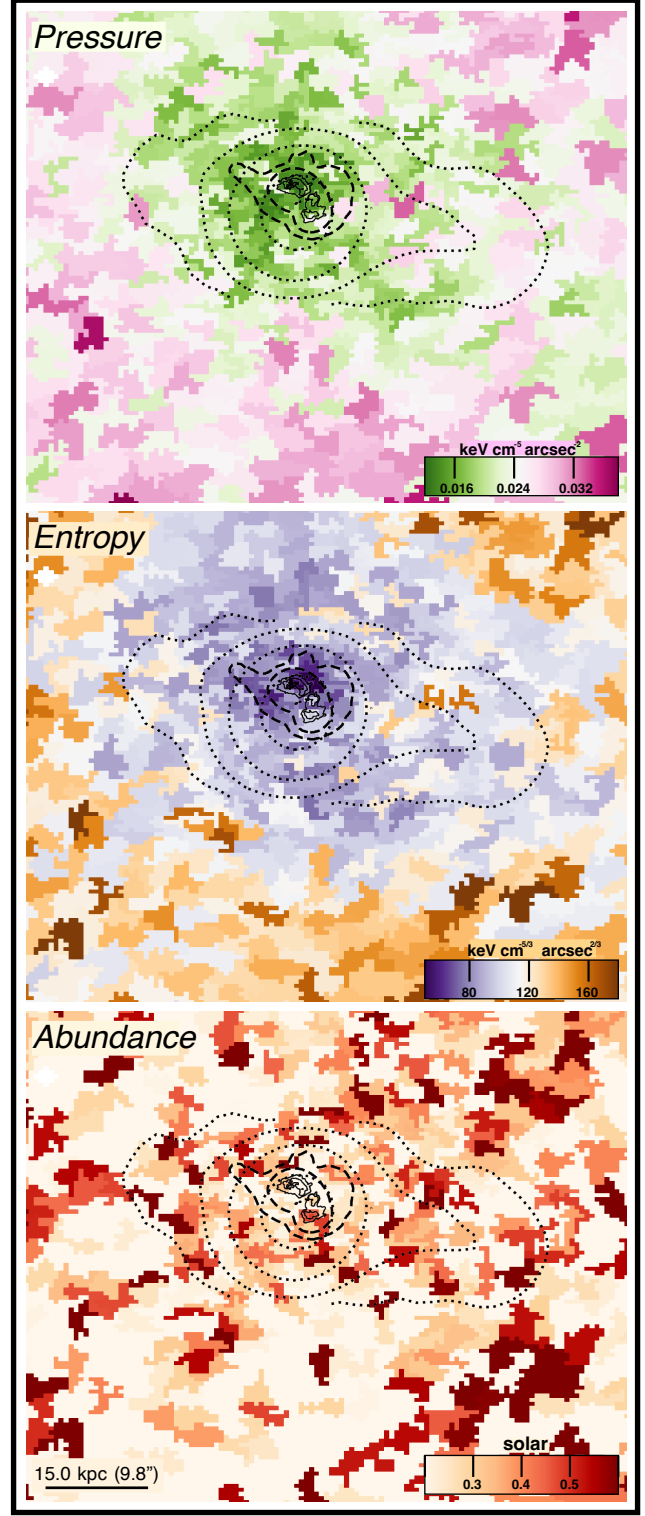


Figure 5. Views of the central 65 kpc of the pressure, entropy, and abundance maps shown in Figures ???. The hot arc is associated with elevated pressure, entropy, and abundance.

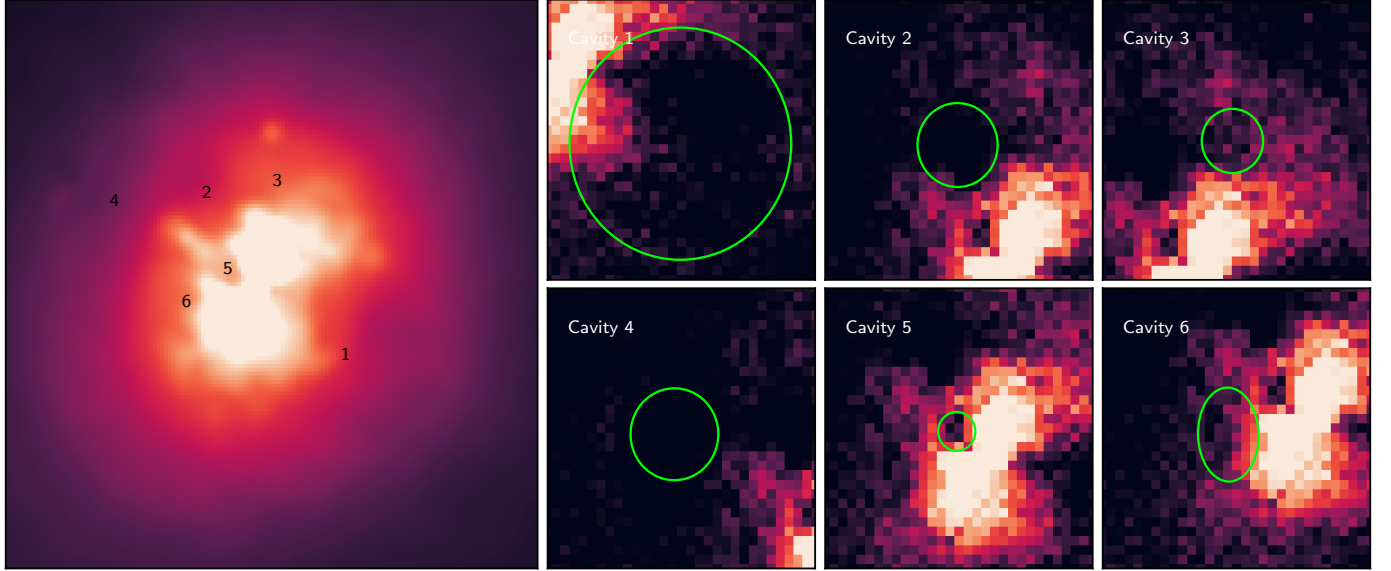


Figure 6. Gaussian smoothed X-ray map of Abell 2597 (left) showing six identified X-ray cavities labeled 1–6. These cavities correspond to depressions in the X-ray surface brightness, indicative of AGN-driven outflows displacing the intracluster medium. The right panels show zoomed-in views of each cavity, outlined in green.

through the ICM to its current projected position in the plane of the sky. The cavity’s age is then estimated as $t_{\text{cav}} = R/v$, where R is the projected distance of the cavity from the ICM peak and v is the bubble’s rise velocity.

To estimate v , we consider two characteristic velocities: the sound speed c_s , which serves as an upper limit on gas motions within the ICM, and the terminal velocity v_t , which accounts for the impact of the ICM’s ram pressure on the buoyancy force. We estimate c_s using $c_s = \sqrt{\gamma kT/\mu m_p}$, where the adiabatic index for a monatomic gas $\gamma = 5/3$, m_p is the proton mass, and the mean molecular weight $\mu = 0.62$.

We calculate v_t following Churazov et al. (2001) as $v_t = \sqrt{\frac{2gV}{SC}}$, where V is the bubble’s volume, S is its cross-sectional area, $C = 0.75$ is the drag coefficient, and g is the gravitational acceleration. We model each cavity as either a spherical or ellipsoidal volume using the values listed in Table ???. Following Bîrzan et al. (2004), we calculate g using the stellar velocity dispersion of the BCG, under the approximation that the galaxy is an isothermal sphere: $g \approx 2\sigma^2/R$, where $\sigma = 350 \text{ km s}^{-1}$ is the median stellar velocity dispersion across the BCG (see Figure 11 in Tremblay et al. (2018)) and R is the projected distance of the cavity from the BCG center.

3.3.4. Cavity Energy

As cavities rise buoyantly through the ICM, they do work on the surrounding medium. We can estimate the

cavity power, P_{cav} , as the ratio of the cavity enthalpy E_{cav} to its age t_{cav} :

$$P_{\text{cav}} = \frac{E_{\text{cav}}}{t_{\text{cav}}} = \frac{4pV}{t_{\text{cav}}},$$

where p is the ambient ICM pressure and V is the cavity volume.

Using the surrounding pressures reported in Table ??, we obtain cavity enthalpies ranging from $\sim 1 - 9 \times 10^{57}$ erg. Employing the average age of each cavity derived from the buoyant rise time and synchrotron age estimates, we calculate cavity powers in the range of $3 - 85 \times 10^{42}$ erg s $^{-1}$. Our values are broadly consistent with those reported by T12b, with the exception of the western large cavity. For this cavity, we find a significantly lower total power of $P_{\text{cav}} = 100 \times 10^{42}$ erg s $^{-1}$, compared to T12b’s value of 170.6×10^{42} erg s $^{-1}$. This discrepancy likely arises from differences in the assumed cavity geometry and age estimates between the two studies. We discuss how this feedback counteracts the ongoing cooling flow in Abell 2597 further in Sections 4.2.3 and 4.2.4.

3.3.5. The X-Ray Channel

The elongated X-ray brightness “channel” identified in Figure 1 lies at the edge of the brightest region in the cluster’s cool core, oriented parallel to the northern radio jet axis. It has a width of 5''.5 (8.3 kpc), a length of 37''.0 (57 kpc), and extends from approximately 60 kpc south of the southern radio jet, running vertically until it reaches the plane of the radio jet’s core, where it curves inward to connect with the gas in the cluster center.

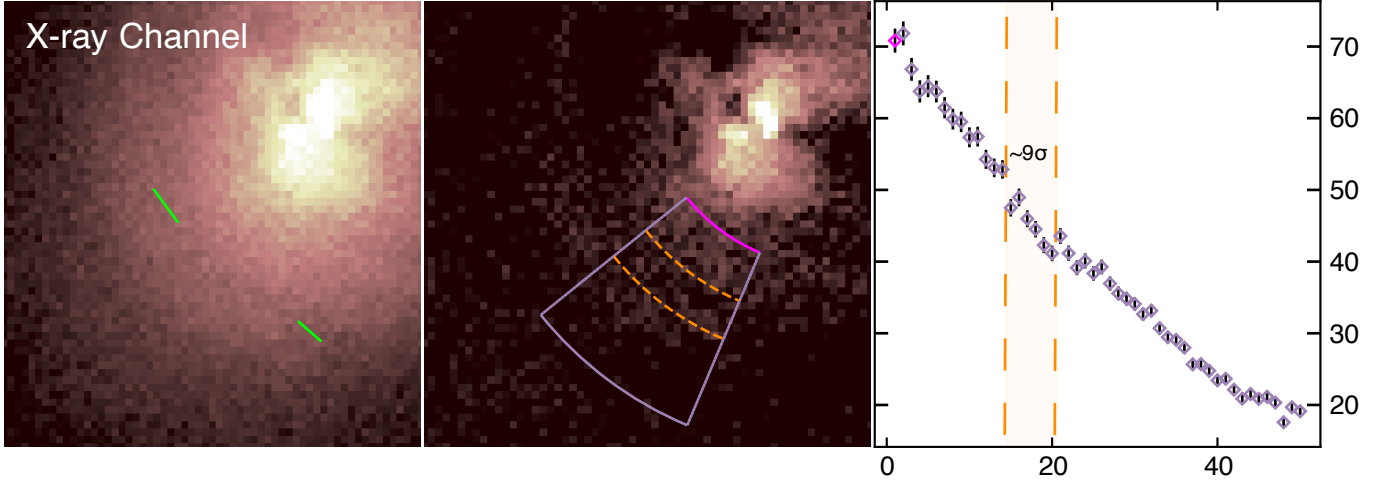


Figure 7. The left panel shows the location of the tentative X-ray channel. The middle panel presents an unsharp masked image to better highlight the surface brightness decrement within the channel. The right panel shows the corresponding surface brightness profile. The channel decrement is detected at 9σ .

The channel also intersects the potential southwestern cold front midway along its length. The temperature maps in Figure 4 show that the channel coincides with a region of slightly hotter gas than in the very core and on the other side of the channel. To analyze the channel’s spectral features, we extracted radial profiles across the region.

Figure 7 shows the resulting surface brightness profile. The surface brightness profile confirms an 9σ or $\sim 20\%$ drop in surface brightness within the region. X-ray channels are thin sheets of lower-density gas within the ICM (Markevitch & Vikhlinin 2007). Assuming rough spherical symmetry for the main cluster body and a complete absence of gas within the 3D channel structure, the sheet’s extent along the line of sight would need to be kpc to produce the observed projected X-ray brightness drop. However, since the channel cannot be entirely devoid of gas, its true extent is likely significantly greater. Similar subtle channels have been observed in the merging cluster Abell 520 (Wang et al. 2016) and the sloshing cool core of Abell 2142 (Wang & Markevitch 2018). We discuss the potential origin of this feature in Section 5.

3.4. 150 kpc - Scale Cocoon Shocks?

To investigate the “cocoon” region further, we created large-scale spectral maps and profiles of the region, obtained through spectral fitting (see Section A.0.1 for details). Figures ?? and ?? presents maps of the temperature, pressure, entropy, and abundance within the ICM. Within the temperature map, the coolest regions ($2 < T < 3.2$ keV) are depicted in blues and greens, while hotter regions are shown in yellows, oranges, and reds. High-pressure areas ($P > 0.04$) are marked by varying shades of pink, while low-pressure regions are colored in different shades of green.

The maps reveal three subtle rings of enhanced temperature and pressure corresponding to the surface brightness edges of the expanding cocoon. The ratio of the shocked regions to the unshocked regions varies between 1.1 and 1.3 across each shock front in both pressure and temperature. The shocks are more easily seen along the major axes of the ellipses rather than the shorter minor axes, with the three distinct rings most clearly visible in the southeastern region of the surface brightness distribution. Within the smallest cocoon, there is an extended region of cooler (< 3.2 keV) emission. In Section 3.3, we discuss the temperature variations in this region further, particularly in relation to its alignment with the 330 MHz radio source. Interestingly, we observe regions of high abundance concentrated around the rings of the cocoon. The entropy map follows the structure of the temperature map, with regions of high temperature correlating with regions of high entropy.

To assess whether the surface brightness edges surrounding the central cavity region each correspond to shock discontinuities, we analyzed the surface brightness profile within the southeastern elliptical sector, shown in the top left panel of Figure 8, where the distinct edges are more prominent and less blended. Surface brightness profiles were extracted using finely binned radial annuli within this sector, maintaining the native resolution to accurately identify large-scale contact discontinuities. The top panel of Figure 8 highlights slight surface brightness discontinuities at each edge, marked by vertical black dashed lines, with distinct density jumps measured at the inner, middle, and outer edges, located at approximately 45 kpc, 75 kpc, and 130 kpc, respectively.

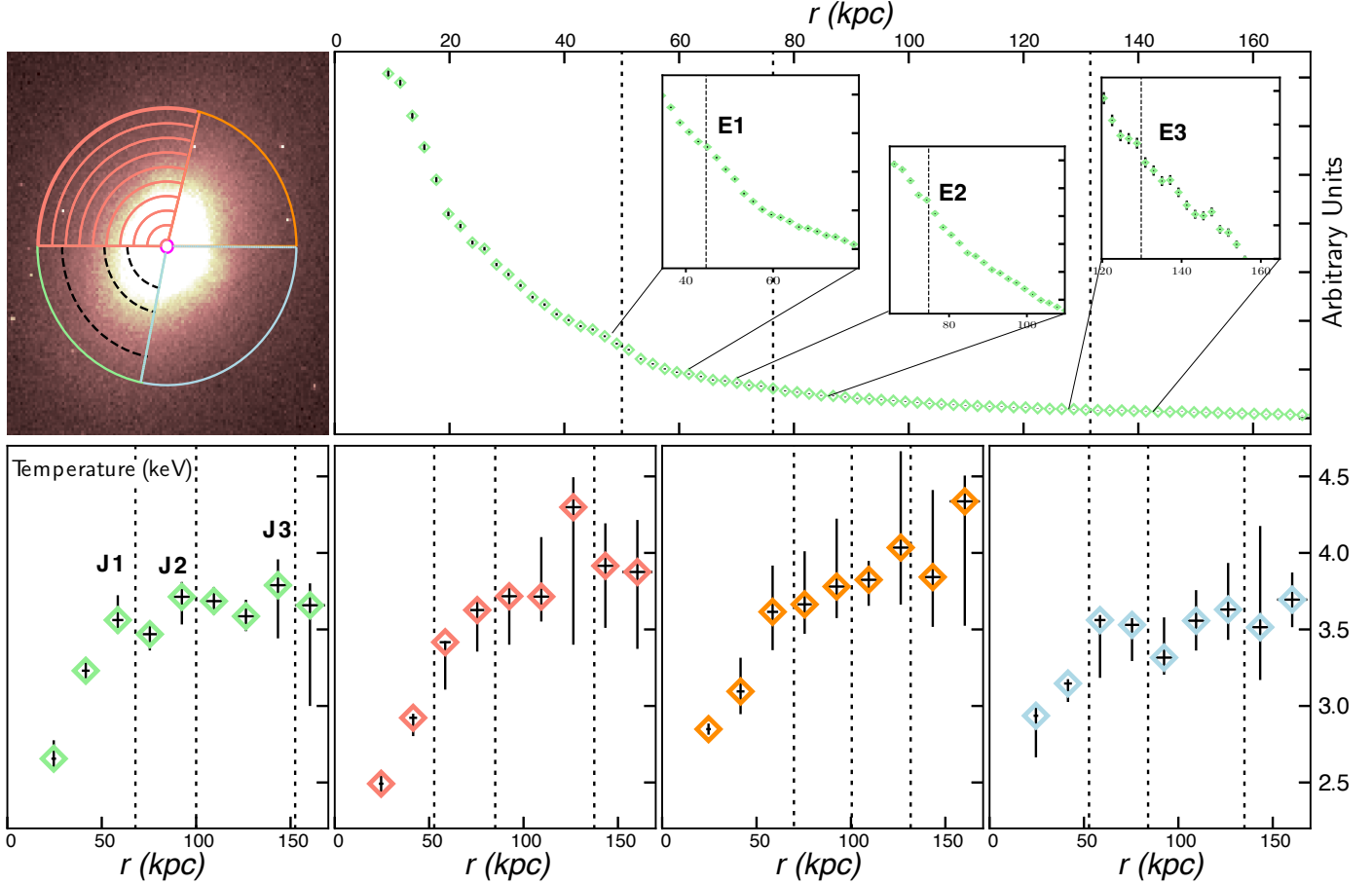


Figure 8. Surface brightness and temperature profiles for the southeastern elliptical sector of Abell 2597, where surface brightness edges are most prominent. Top left: *Chandra* X-ray image with radial wedges used for profile extraction. Dashed circles mark the approximate locations of the three edges at 45 kpc, 75 kpc, and 130 kpc. Top right: Surface brightness profile extracted using finely binned radial annuli, showing distinct discontinuities at each edge (E1, E2, E3), highlighted in the inset panels. Bottom panels: Temperature profiles for each wedge, with vertical black dashed lines indicating the positions of the surface brightness edges. The observed temperature jumps are 1.1 ± 0.03 at the inner edge, 1.07 ± 0.06 at the middle edge, and 1.05 ± 0.1 at the outer edge. While the temperature profiles show subtle jumps, corresponding pressure jumps (not shown) are negligible.

We also extracted and analyzed the temperature and pressure within nine radial bins in each wedge, with counts ranging from 5,500 to 27,000 per bin. The middle panel displays the temperature jumps at each surface brightness edge, indicated by vertical black dashed lines. The southeastern wedge provides the clearest estimates for pre-shock and post-shock temperatures. From the ratio of the pre-shock temperature (T_1) to the post-shock temperature (T_2), we observe temperature jumps of 1.1 ± 0.03 at the inner edge, 1.07 ± 0.06 at the middle edge, and 1.05 ± 0.1 at the outer edge. Although subtle jumps are observed in the temperature profiles, the corresponding pressure profiles (lower panel) show virtually nonexistent pressure jumps compared to the pseudo-pressure map. This discrepancy is likely due to the corrections for actual volume and electron density in the profiles, unlike in the pseudo map.

Nonetheless, the density discontinuities shown in Figure 8 provide tentative evidence for the presence of multiple fronts. However, it is possible that if these discontinuities are indicative of fronts, that rather than shock fronts, we are observing successive waves of a cold front. However, interpreting this feature as a cold front presents certain challenges, which we explore further in Section 4.2.4.

For now, we interpret the edges as shock fronts and estimate the Mach number, \mathcal{M} , based on the observed temperature jumps, using the relation from Landau & Lifshitz (1959) and Sarazin et al. (2016):

$$\mathcal{M} = \sqrt{\frac{(8 \cdot \frac{T_2}{T_1} - 7) + \sqrt{(8 \cdot \frac{T_2}{T_1} - 7)^2 + 15}}{5}}, \quad (1)$$

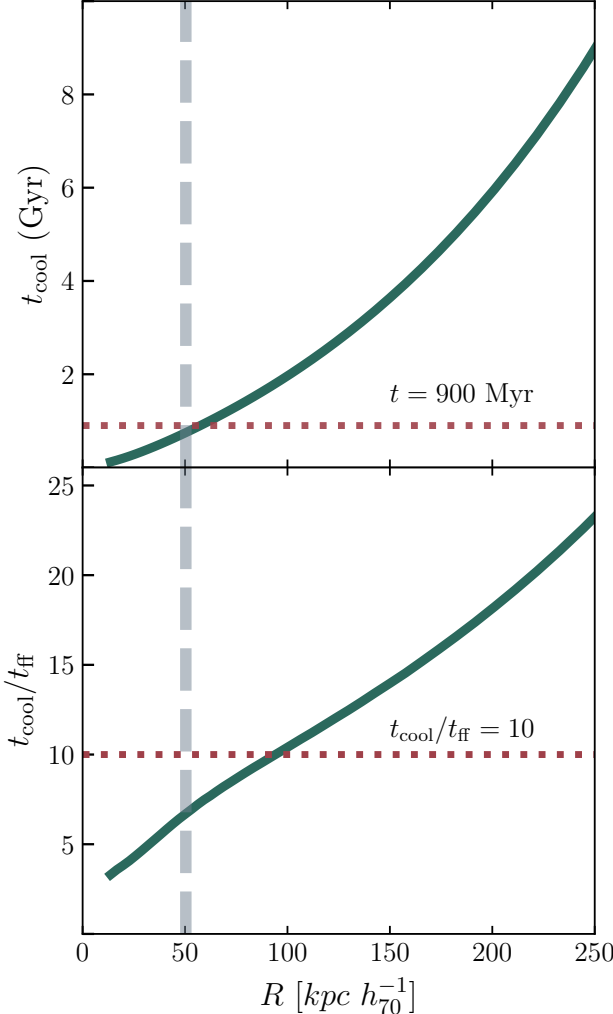


Figure 9. Radial timescales describing the thermodynamic state of the ICM. The top panel displays the cooling time t_{cool} , and the lower panel shows the ratio of the cooling time to the free-fall time t_{ff} .

where T_1 is the pre-shock temperature and T_2 is the post-shock temperature. We obtain Mach numbers 1.22, 1.15, and 1.12 across the inner, middle and outer edges, respectively, classifying them as very weak shock fronts.

4. HEATING THE RAPIDLY COOLING ICM

The presence of a strong cooling flow in Abell 2597 motivates an investigation into the gas cooling, heating and accretion processes onto the central galaxy.

4.1. Thermal Instabilities and Residual Precipitation

In the classical picture of gas cooling within the ICM, thermal instabilities drive the condensation of cooler, denser gas phases. As the ICM radiates energy, certain regions become unstable, leading to runaway cooling where gas rapidly contracts and forms denser clouds within the hotter medium. This process is analogous to

rain cloud formation on Earth, where water vapor condenses into liquid droplets in localized regions due to changes in temperature and pressure. Similarly, thermal instabilities cause localized regions of the ICM to cool and condense into colder gas clouds, rather than causing uniform cooling across the entire cluster (McNamara & Nulsen 2012).

Several key timescales are predicted to govern the onset of thermal instabilities within the ICM. The free-fall time, t_{ff} , describes the time it takes for gas to collapse onto the central galaxy under its own gravity. In the “circumgalactic precipitation” model, when $t_{\text{cool}}/t_{\text{ff}}$ falls below a critical threshold (typically around 10), local thermal instabilities trigger cooling and condensation (Voit et al. 2017). Figure 9 shows the radial profile of $t_{\text{cool}}/t_{\text{ff}}$ in Abell 2597, revealing that the ratio falls below 10 within the cooling radius, indicating ongoing cooling and condensation.

As one of the most extensively studied cool-core clusters across the electromagnetic spectrum, Abell 2597 provides a detailed view of cooling processes across all temperature phases—from the hot X-ray emitting gas studied here to the coldest 100 K gas observed with ALMA (Tremblay et al. 2016). Figure ?? overlays the mapped phases as contours on the central X-ray map, following the “S”-shaped structure seen in the X-ray surface brightness distribution. This alignment supports the concept of a multiphase cooling cascade, where the hot X-ray bright gas cools and condenses into progressively colder phases.

In the top panel of Figure 9, we plot the cooling time as a function of radius within the cluster. Within the X-ray cavity region, the enclosed hot gas mass should cool within approximately 900 Myr, corresponding to a classical cooling rate of $\sim 560 M_{\odot} \text{yr}^{-1}$. Observations, however, suggest significantly lower cooling rates. Using *XMM* Reflection Grating Spectrometer spectra, Fabian et al. (2023) estimated an X-ray cooling rate of $\sim 67 M_{\odot} \text{yr}^{-1}$ after accounting for intrinsic absorption in the spectral fits, which captures soft X-ray emission hidden by photoelectrically absorbing cold clouds and dust near the centers of BCGs. This aligns with cooling rates inferred from O VI $\lambda 1032$ ultraviolet emission detected by FUSE, which, assuming the O VI $\lambda 1032$ emission originates from thermal gas at $\sim 7 \times 10^5$ K, suggests a cooling rate of $\sim 40 M_{\odot} \text{yr}^{-1}$ within < 46 kpc, or up to $150^{+140}_{-100} M_{\odot} \text{yr}^{-1}$ when corrected for dust extinction (Oegerle et al. 2001).

Recent HST COS observations, which provide higher resolution UV data than FUSE, also detected the O VI $\lambda 1032$ line, but within the central 2 kpc of the cluster (Vaddi et al., in prep). From the line’s luminosity, they

estimate a cooling rate of $15.6 \pm 0.9 M_{\odot} \text{yr}^{-1}$ within the nuclear region. Assuming this rate holds roughly consistent out to ~ 20 kpc, where ALMA derived a cold gas mass of $3.2 \pm 0.1 \times 10^9 M_{\odot}$ (Tremblay et al. 2016, 2018), the residual cooling flow could fill the $3 \times 10^9 M_{\odot}$ gas reservoir within the estimated 190 Myr cooling time at that radius, suggesting ongoing replenishment of the cold gas could be consistently replenished by the ongoing residual cooling flow.

4.2. AGN Feedback History and Power

The most obvious candidate for reducing the $\sim 500 M_{\odot} \text{yr}^{-1}$ cooling flow to the moderate $\sim 15 M_{\odot} \text{yr}^{-1}$ cooling rate is AGN feedback. Abell 2597 is particularly notable for hosting an extensive network of ghost cavities, a phenomenon rarely observed in such abundance in nearby clusters. Previous analysis of these cavities by T12a suggested they might originate from an AGN that alternates between active and quiescent phases or transitions between high and low activity modes. The estimated cycling time for these AGN phases, on the order of 10^7 to 10^8 years, aligns with findings from other studies on the AGN duty cycle (see Figure 15 in Vantyghem et al. 2014).

4.2.1. Cavity Origins

C05 estimated the minimum age of the 330 MHz radio source associated with the teardrop-shaped cavity to be between 8×10^6 and 5×10^7 years. The upper limit is consistent with the buoyant rise time of the cavity, suggesting the radio source likely propagates with the X-ray gas. However, the lower limit raises the possibility that the radio source is younger than the cavity it fills. Tremblay et al. (2012b) noted this could occur if adiabatic and/or inverse Compton losses dominate over synchrotron processes, but considered it less likely due to the absence of fast shocks, which our deeper *Chandra* observations also confirm.

Interestingly, the teardrop cavity appears to be split into two distinct regions, as revealed by the surface brightness, temperature, entropy, and pressure maps. This feature could result from turbulent gas motions in the ICM shearing the bubble into two components, a phenomenon observed in simulations of the Perseus cluster (see Figure A5 in Fabian et al. 2022b). Such motions could also explain the depression extending below the southwestern ghost cavity, which aligns with the direction of the teardrop cavity and may represent a sheared-off portion of the bubble during its expansion. However, the exact origin of these ICM motions remains unclear, as the X-ray map does not reveal any obvious cold fronts.

The northeastern cavity is clearly associated with the northern 8.4 GHz radio jet, while the southern radio lobe may have been deflected by interaction with the surrounding medium (Koekemoer et al. 1999; Tremblay et al. 2018), linking the cavity created by the 330 MHz source to the younger emission. The northeastern and outer northeastern ghost cavities (features 4 and 6) appear aligned with the axis of the eastern lobe of the 330 MHz source, suggesting they were excavated by this older emission. However, the lobe does not currently extend to these features, suggesting the radio emission may have faded since their formation. Additional, higher-quality radio observations beyond those currently available in the GMRT archive are needed to confirm the origins of these cavities and to better understand their evolution.

4.2.2. Episodic AGN Activity

Of all the cavities observed, the cavity associated with the 330 MHz source is the oldest, with a buoyant rise time of 1.8×10^8 years. Given this relatively short timescale, C05 found that it remained plausible that none of the cavities were truly “ghost” cavities, but rather products of the current AGN feedback episode. Previous radio observations, limited in frequency coverage and sensitivity, precluded a definitive answer to this question. Similarly, the archival GMRT data do not allow us to confidently determine the age gradient of the radio emission filling the teardrop cavity or the other identified cavities using spectral indices. Nevertheless, we attempt such an analysis to estimate the relative ages of different cavity components, which may indicate whether they were excavated during separate AGN outbursts.

During an AGN outburst, jets not only inflate cavities but also drive weak shocks through the ICM. We identify three distinct surface brightness edges in Section 3.4, each corresponding to a front expanding outward from the AGN. However, as previously discussed, the nature of these fronts remains somewhat ambiguous. In Figure 8, the temperature versus radius profiles for each sector reveal that at the locations of each surface brightness edge, the temperature slightly decreases with increasing radius—behavior that is contrary to what we would expect for cold fronts, where gas inside the front should be cooler than the gas outside.

Shock models, on the other hand, predict a modest temperature increase, typically around 5%, just behind the shock front. This is more consistent with the temperature profiles shown in Figure 8, where we observe slight but distinct temperature jumps across each surface brightness edge. Additionally, the alignment be-

tween these edges and the radio lobes suggests a direct association with radio plasma outflows, supporting the interpretation that these edges are indeed weak shock fronts driven by the AGN.

Cold fronts generally arise from contact discontinuities between cooler, denser gas moving through a hotter medium, making it challenging to explain the presence of multiple concentric cold fronts. Typically, cold fronts show a sharp density discontinuity in one direction (see Markevitch & Vikhlinin (2007) for a review) and do not usually extend uniformly around the cluster center, unless the motion of the gas is predominantly along our line of sight. In contrast, the nearly circular geometry of the observed fronts is naturally explained by an expanding cocoon of radio plasma, where the AGN outburst drives shocks into the ICM.

Given the slight temperature jumps, the correlation with radio features, and the circular geometry of the fronts, we conclude that these edges are weak shock fronts rather than cold fronts. Furthermore, regions of high entropy and abundance are concentrated along the rings of the cocoon, consistent with predictions that AGN-driven outflows lift metal-enriched gas to large radii as they expand through the cluster (Kirkpatrick et al. 2009; Simionescu et al. 2009).

To estimate the ages of the potential shock fronts (t_{age}), we calculate the time required for the shocks to travel from the cluster center to their current positions (r_{sh}) using their observed Mach numbers (\mathcal{M}), based on the following relation:

$$t_{\text{age}} = \frac{r_{\text{sh}}}{\mathcal{M} c_s}, \quad (2)$$

where c_s is the sound speed of the undisturbed gas ahead of the shock, determined using the temperature outside the shock front. It's important to note that this approach may slightly overestimate the actual age of the shock by about 10–20% (as noted by Russell et al. (2010)), since the shocks likely started with higher Mach numbers when first launched.

Applying this approach, we estimate the ages of the shock fronts to be approximately 50 Myr for the inner shock, 80 Myr for the middle shock, and 100 Myr for the outer shock. The outer shock's age, around 1×10^8 years, aligns with the estimated age of the oldest radio source, suggesting that the expansion of the oldest radio lobe could have produced it. If the inner shocks are due to later outbursts from the radio source, their ages imply an average cycle time of $\sim 2 \times 10^7$ years in between outbursts, consistent with findings from other cool core systems with multiple rounds of AGN feedback (Vantyghem et al. 2014).

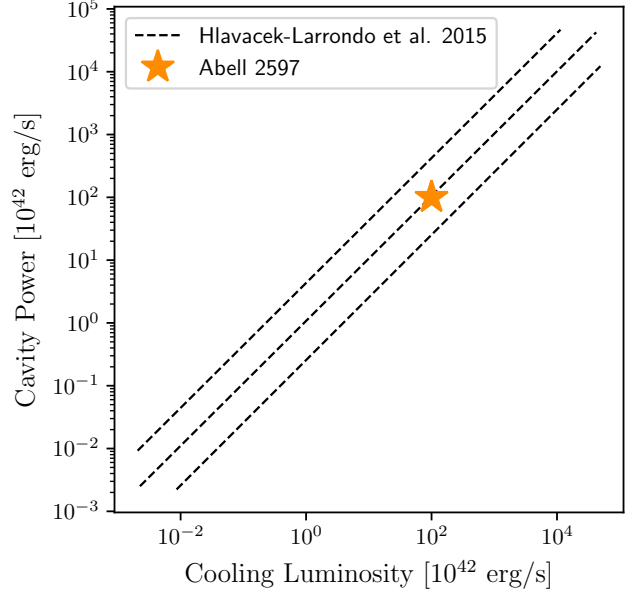


Figure 10. Cavity power versus cooling luminosity for Abell 2597 (orange star), plotted alongside the best-fit relation from Hlavacek-Larrondo et al. (2015) (dashed lines). Abell 2597 lies along the typical trend observed in cool-core clusters, where AGN cavity power scales with the radiative cooling luminosity of the intracluster medium.

4.2.3. Cavity Heating and the Role of the Hot Arc

At a cluster temperature of 3.5 keV, the total cooling luminosity is $L_{\text{cool}} \approx 1 \times 10^{44}$ erg s⁻¹, closely matching the power output of the expanding X-ray cavities, $P_{\text{cav}} \sim 2 \times 10^{44}$ erg s⁻¹ (see Table ??). This consistent alignment, first reported in T12a and confirmed here, strongly suggests that AGN feedback plays a key role in offsetting radiative cooling in the cluster's core. Such behavior mirrors that seen in nearly all nearby cool-core clusters (Fabian 2012), with Abell 2597 fitting neatly along the $P_{\text{cav}} - L_{\text{cool}}$ relation from Hlavacek-Larrondo et al. (2015) (see Figure 10).

While the correlation between cavity power and cooling luminosity is well-established, the exact mechanism by which energy from the cavities heats the ICM remains elusive. The detection of a hot arc bordering the inner edge of the largest X-ray cavity within the cluster may offer a long-sought-after glimpse into this process. Previously identified in T12a at a signal-to-noise ratio of ≤ 30 , the arc was tentatively linked to interactions between the cavity and surrounding gas.

T12a explored several potential explanations for the origin of the hot arc, including: (1) a superposition of foreground features or localized soft X-ray absorption, (2) displacement of cooler gas by the 330-MHz radio bubble, or (3) a direct signature of cavity heating. To investigate the possibility that the arc is associated with

soft X-ray absorption due to a higher intrinsic column density, we extracted profiles across the arc as shown in Figure 13, and fit the extracted spectra by fixing the abundance at 0.4 (the median for the region) while allowing the temperature, normalization, and column density to vary. We find that the column density shows no significant variation across the region, making it unlikely that the arc represents a site of elevated soft X-ray absorption. Regarding scenario 2, the X-ray spectral maps shown in Figure 4 and 5 reveal that the region encompassing the hot arc is also coincident with elevated entropy and pressure, inconsistent with the presence of displaced cool gas. Instead, our deeper observations support the interpretation that the hot arc is a direct result of cavity-driven heating.

In AGN-driven cavity heating models, the enthalpy of buoyantly rising cavities dissipates into the surrounding gas, thermalizing the ambient medium as it refills the cavities' wakes (McNamara & Nulsen 2007, 2012). The position and morphology of the hot arc, bordering the inner edge of the western cavity (Figure 4), align well with this scenario. The median temperature of the gas in the arc is approximately 0.5 keV hotter than the coolest gas in the core and 0.2 keV hotter than the surrounding ICM outside of it. These models suggest that as the cavity rises, gravitational potential energy is converted into kinetic energy, which then dissipates as heat into the surrounding medium, driving the observed temperature enhancements.

4.2.4. Shock Energy

The energy released during an AGN outburst is divided between the internal energy stored in the cavities and the work done by the cavities as they expand, which in turn drives the shock. Given the detection of three potentially distinct shock edges, these shocks, if real, were likely driven over 3 cycles of AGN activity. Following Section 5.6 of Randall et al. (2010), we can estimate the total energy E imparted to the ICM from each shock as:

$$E \approx PV(f_P - 1), \quad (3)$$

where V is the gas volume contained within the shock front, P is the pressure across the front, and $f_P = (P + \Delta P)/P$ describing the ratio of the post- and pre-shock pressure.

Since direct pressure jumps are not clearly detected for the weak shock fronts, we can relate f_P to the Mach number from the Rankine-Hugoniot shock jump conditions as

$$f_P = \frac{2\gamma\mathcal{M}^2 - (\gamma - 1)}{\gamma + 1}, \quad (4)$$

where $\gamma = 5/3$ and the Mach number is taken from that estimated from the observed density and temperature jumps.

The pre-shock pressure for each ring is taken from the pressure closer to the central region. By considering an ellipsoidal volume for the region enclosed by each shock front, we estimate the energy to be approximately 3×10^{59} erg per front, leading to a total shock energy on the order of $\sim 1 \times 10^{60}$ erg. This corresponds to an average power output of 1×10^{44} erg s $^{-1}$, which is consistent with the total cavity power and the cooling luminosity.

Because we assume a constant Mach number over each shock's life, the energy calculated using this formula may slightly underestimate the total shock energy, as the Mach number likely would have been higher during earlier stages of the shock's development. Nevertheless, the shock energy derived from this approach generally aligns within a factor of a few with estimates from hydrodynamical simulations of a central point explosion, as derived from surface brightness profiles (e.g., Randall et al. 2010).

4.2.5. Ineffiecient Heating

Although the cavities and potential shocks contribute significantly to the cluster's energy budget, each with an estimated power of $\sim 10^{44}$ erg/s, they are likely insufficient to fully quench the cooling flow. If all the energy were directed toward offsetting radiative losses, complete suppression of cooling might be achievable. However, several factors make this scenario unlikely.

First, weak shocks typically deliver only a small fraction of their energy—5–10% in systems like NGC 5813 (Randall et al. 2010)—as heat within the cooling radius. This limited energy input means shock heating alone cannot counterbalance radiative cooling, particularly near the observed shock fronts. Furthermore, sustained thermal balance requires heating not only to inject energy but also to raise the gas's entropy enough to offset the continual entropy reduction caused by cooling. While the shocks at 50 kpc, 80 kpc, and 100 kpc correspond to regions of elevated entropy, their localized effects are insufficient to prevent cooling across the cluster. For instance, the cooling time of gas just outside the 50 kpc shock front is approximately 800 Myr, which remains short enough to allow runaway cooling over the cluster's lifetime.

This inefficiency is consistent with the broader argument that while bubble enthalpy and shock heating play a significant role, they likely do not fully offset radiative losses in the cluster core. This conclusion is further supported by the persistence of residual cooling in Abell

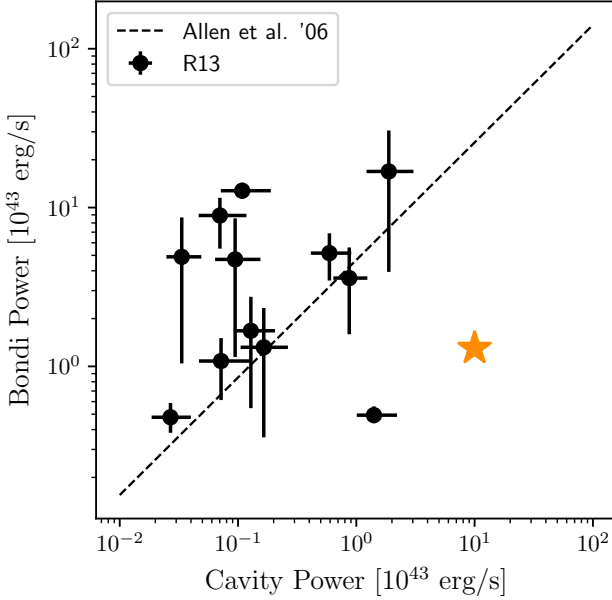


Figure 11. Plot of cavity power versus Bondi power, adapted from Russell et al. (2013) and Allen et al. (2006). Abell 2597 is represented by the orange star. The Bondi power for Abell 2597 is significantly lower than the required cavity power, suggesting that Bondi accretion may not be the predominant mechanism through which the AGN is fueled.

2597, as evidenced by the presence of cooler gas phases cospatial with the coldest X-ray bright gas.

4.3. The Supermassive Black Hole’s Fuel Supply

The coexistence of hot, warm, and cold gas phases in the core of Abell 2597 naturally raises the question: which phase primarily fuels its supermassive black hole? Given the sustained AGN activity, a continuous fuel supply is necessary to maintain its power output. At the scale of the Bondi radius, the two potential fueling mechanisms invoked in galaxy formation studies can be broadly classified into two modes(Kereš et al. 2005): hot mode and cold mode accretion.

In the hot mode, ~ 1 keV gas is directly accreted onto the SMBH. To estimate an upper limit on the Bondi accretion rate within 760 pc, the native *Chandra* resolution, we use Equation 6 from Rafferty et al. (2006), which relates the accretion rate to the electron density (n_e), gas temperature (T), and black hole mass (M_{BH}) as:

$$\dot{M}_B = 0.012 \left(\frac{T}{\text{keV}} \right)^{-3/2} \left(\frac{n_e}{\text{cm}^{-3}} \right) \left(\frac{M_{\text{BH}}}{10^9 M_{\odot}} \right)^2 \text{M}_{\odot} \text{yr}^{-1}, \quad (5)$$

To update the black hole mass estimate from T12b, we use the spatially resolved MUSE data presented in Tremblay et al. (2018) to adopt a stellar velocity dis-

persion of $\sim 290 \text{ km s}^{-1}$ within the nucleus and the $M_{\text{BH}} - \sigma$ relation from McConnell et al. (2011) for elliptical galaxies, we calculate $M_{\text{BH}} = 1.3 \times 10^9 M_{\odot}$. This gives a Bondi radius of $\sim 22 \text{ pc}$.

Since *Chandra* cannot resolve the Bondi radius in A2597, we extrapolate n_e and T to this scale using a beta model for the density profile (Russell et al. 2013) and assume the temperature at the Bondi radius is approximately one-fourth of the central temperature from Table 3. Using $n_e = 0.11 \text{ cm}^{-3}$ and assuming that the temperature at the Bondi radius is approximately one-fourth of the central temperature reported in Table 3, we estimate the Bondi accretion rate at 760 pc to be $\dot{M}_{B,760\text{pc}} \sim 3.6 \times 10^{-3} M_{\odot} \text{ yr}^{-1}$. The Eddington accretion rate, calculated using Equation 5 in Rafferty et al. (2006) and $\epsilon = 0.1$, results in an accretion rate of $\sim 30 M_{\odot} \text{ yr}^{-1}$. Both the Bondi and cavity-power-derived accretion rates are sub-Eddington, consistent with T12b.

To explore the implications for AGN fueling, we calculate the Bondi power as $P_{\text{Bondi}} = \eta \dot{M}_{\text{Bondi}} c^2$, where $\eta = 0.1$ represents the radiative efficiency. Using our estimate for the Bondi accretion rate, this yields $P_{\text{Bondi}} \sim 2 \times 10^{43} \text{ erg s}^{-1}$. Figure 11 compares the Bondi power to the cavity power for A2597, along with data from Russell et al. (2013). In A2597, the Bondi power falls an order of magnitude below the estimated cavity power, suggesting that hot mode accretion alone may not provide sufficient fuel to power the observed AGN activity. This result is consistent with the findings for M87, where *Chandra* resolves the Bondi radius, yet the Bondi power is two orders of magnitude below the jet mechanical power (Russell et al. 2015).

Early studies of nearby elliptical galaxies, such as Allen et al. (2006), reported a correlation between Bondi accretion power and AGN jet power, inferred from the enthalpy of jet-blown cavities. However, this correlation is subject to significant uncertainties, including projection effects and assumptions about subsonic cavity inflation. A subsequent analysis by Russell et al. (2013) using a larger sample found a weaker correlation, further emphasizing that Bondi accretion alone cannot fully account for the observed AGN energetics. In Abell 2597, as in other systems, additional fueling mechanisms, such as cold mode accretion, may be required to bridge the gap between Bondi power and the energy output of the AGN.

In cold mode accretion, thermally unstable gas cools and condenses out of the hot ICM, forming dense clouds and filaments. In the Chaotic Cold Accretion (CCA) model (Gaspari et al. 2018), the ratio of t_{cool} to the eddy turnover time, t_{eddy} , can serve as an indicator of

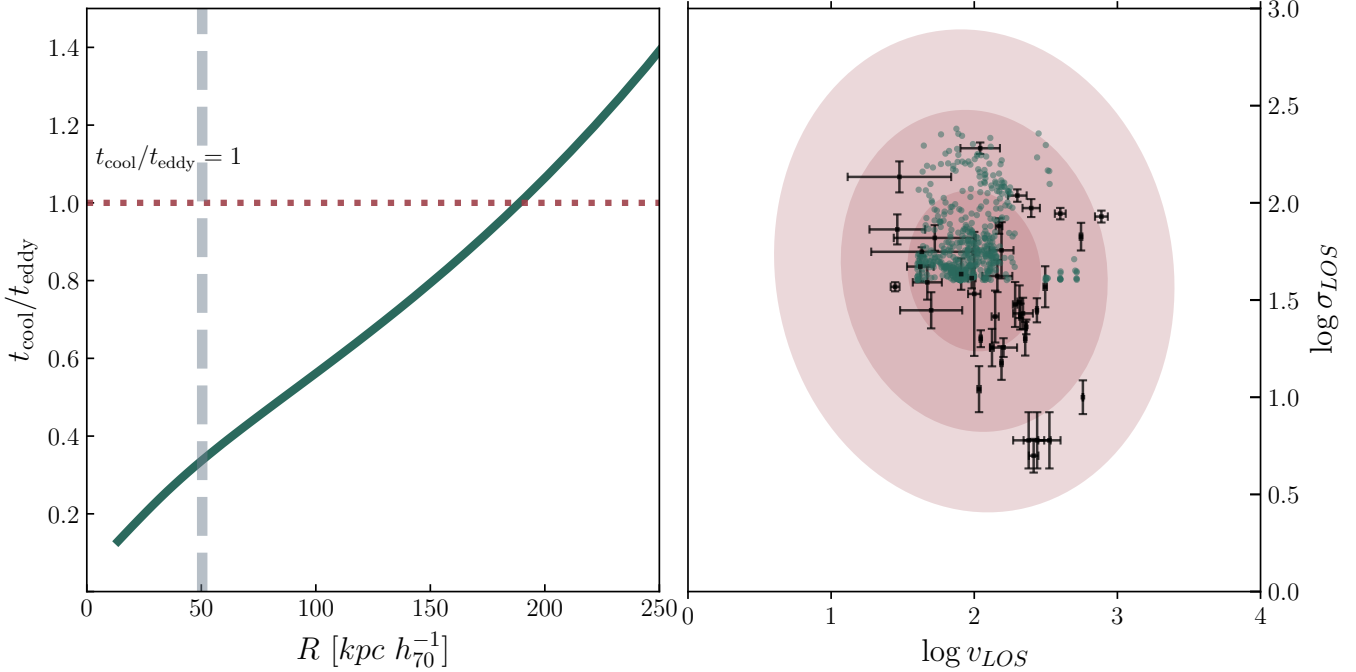


Figure 12. Ratio of the cooling time to the eddy turnover time ($t_{\text{cool}}/t_{\text{eddy}}$; left) and the k-plot (right) for Abell 2597. The left panel shows $t_{\text{cool}}/t_{\text{eddy}}$ as a function of radius, with the vertical dashed line marking the cooling radius and the horizontal dotted line indicating $t_{\text{cool}}/t_{\text{eddy}} = 1$, below which thermal instabilities are expected to form. The right panel presents the k-plot, displaying the distribution of gas in line-of-sight velocity versus velocity dispersion, where the cold-phase points are derived from archival ALMA CO (2-1) observations of the molecular gas published in Tremblay et al. (2018). The concentration of cold-phase points in the central infalling zone aligns with predictions from the chaotic cold accretion, rather than Bondi accretion.

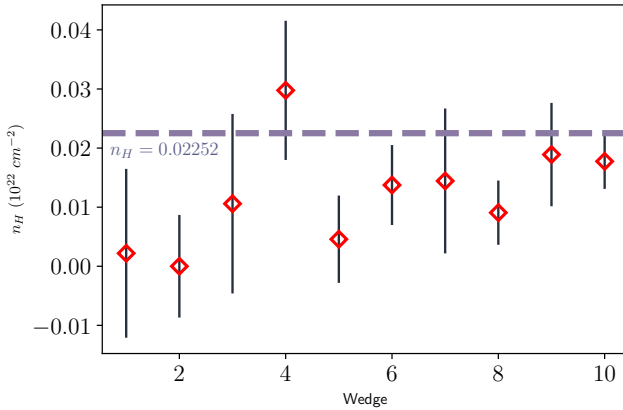


Figure 13. Hydrogen column density (N_{H}) measured across different wedges in the hot arc region. The dashed line represents the hydrogen column density estimated by the NASA column density tool, $N_{\text{H}} = 0.02252 \times 10^{22} \text{ cm}^{-2}$. N_{H} remain roughly consistent across all wedges, suggesting that the hot arc is not a region of higher intrinsic N_{H} , disfavoring the possibility of enhanced soft X-ray absorption in the hot arc region.

thermal instability. The eddy turnover time is defined as:

$$t_{\text{eddy}} = 2\pi \frac{r^{2/3} L^{2/3}}{\sigma_{v,L}}, \quad (6)$$

where L is the injection length scale of the turbulence and $\sigma_{v,L}$ is the velocity dispersion. Given that these parameters are difficult to observe directly in the ICM, we use the velocity dispersion of the southern CO filament as a proxy for ICM turbulence. The filament's median velocity dispersion is $\sim 50 \text{ km s}^{-1}$ (Tremblay et al. 2018), and we correct for the three-dimensional velocity dispersion, adopting $\sigma_{v,L} \approx 80 \text{ km s}^{-1}$. We estimate the injection length scale L to range from 12 to 70 kpc, consistent with the observed CO emission and X-ray/radio cavity extent.

The left panel of Figure 12 shows that $t_{\text{cool}}/t_{\text{eddy}}$ approaches unity across the region where CO is observed, supporting the idea that the ICM is thermally unstable and rapidly cooling out to at least 60 kpc.

If these cold structures can lose or maintain low angular momentum, they can “rain” onto the central SMBH, potentially fueling it at rates exceeding those of Bondi accretion alone (Pizzolato & Soker 2005; Gaspari et al. 2012). CCA further posits that turbulence within the ICM can enhance this cold gas accretion, leading to in-

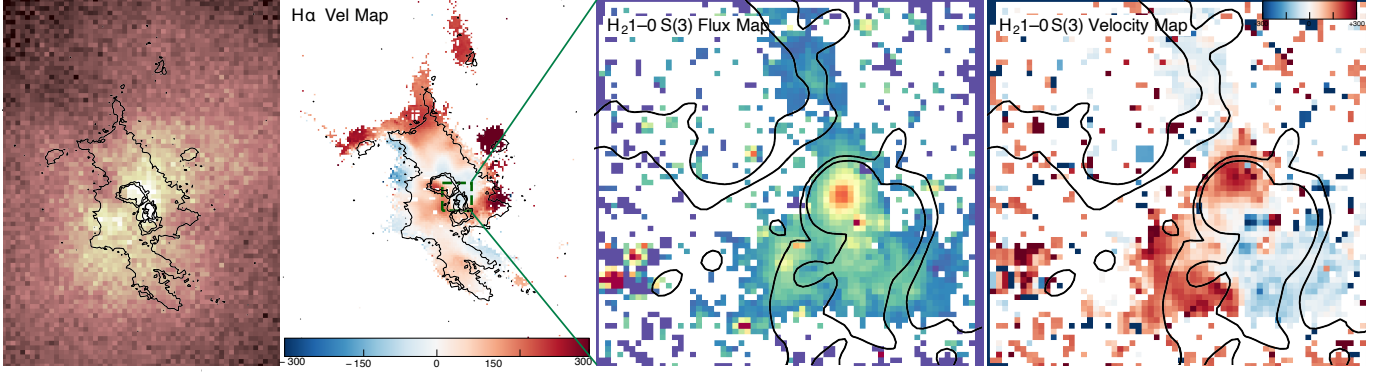


Figure 14. The distribution and kinematics of the multiphase gas in the core of Abell 2597. Left two panels: *Chandra* X-ray map with blsck H α contours, showing warm gas draped around the rims of the southwestern teardrop-shaped cavity and northern ghost cavities. The dashed green square marks the region shown in the SINFONI maps (right two panels). The SINFONI H $_2$ (1-0) S(3) flux map (middle right) reveals molecular gas aligned with the edges of the northern radio lobe and deflected southern lobe. The velocity map (right) shows molecular gas kinematics influenced by the radio lobes.

intermittent boosts in SMBH accretion rates by up to two orders of magnitude (Gaspari et al. 2016).

To examine signatures of CCA in Abell 2597, we re-created the k-plot diagnostic from Gaspari et al. (2018), shown in the right panel of Figure 12 which explores the relationship between velocity dispersion and radial distance of the multiphase gas. Under the CCA scenario, we expect to observe a decrease in velocity dispersion toward the cluster center, along with increased scatter. This behavior would manifest as a combination of narrow and broad spectral line components: narrow lines tracing the infall of dense, cold clouds, and broader lines indicating more distant, turbulent gas. Using spatially resolved ALMA data from T18, we observe that the cold clouds cluster near the center of the plot, suggesting the presence of infalling cold clouds toward the SMBH, which aligns with the results of Tremblay et al. (2016), who detected three deep, narrow absorption features against the SMBH’s continuum (see their Figure 3), interpreted as “shadows” cast by such infalling clouds. These potentially massive clouds ($10^5 - 10^6 M_\odot$) could supply an accretion rate of ~ 0.1 to a few $M_\odot \text{ yr}^{-1}$ if they are falling directly towards the black hole. However, if most of the clouds are instead on non-circular orbits, the fueling rate would depend on their angular momentum and the efficiency of angular momentum loss mechanisms.

In a future paper, we will present the deep *Chandra* data alongside new JWST MIRI and NIRSPEC observations of the nucleus of Abell 2597. This will allow us to better constrain the gas mass budget within the Bondi radius, and determine the relative contributions of cold and hot gas to the accretion process.

4.4. The Multiphase Fountain

4.4.1. Stimulated Uplift

Although the residual cooling rate is sufficient to supply the entire cold gas mass reservoir, it is clear that multiple rounds of AGN feedback have significantly shaped the distribution of this gas, as noted in Section 4.2 of (Tremblay et al. 2018). The left panel of Figure 15 shows that the warm gas traced by H α is cospatial with the outer X-ray cavities, draping around the rims of the southwestern teardrop-shaped cavity, as well as the northern ghost cavities. In the nuclear region, the right panel of Figure 15 shows the warm molecular gas probed by the vibrational H $_2$ (1-0) transition similarly draped around the edges of the northern radio lobe and deflected southern radio lobe, suggesting that the active radio source is dynamically shaping the inner gas reservoir. The spatial correlation between the multiphase gas and the cavities implies two possibilities: (1) the gas has been entrained and uplifted by the jetted outflows, and/or (2) it has formed *in situ* from cooling warm outflows.

Tremblay et al. (2018) primarily explored the first scenario, where pre-existing cold gas is uplifted by buoyant X-ray cavities. They demonstrated that the mechanical energy of the cavity network is sufficient to lift the entire cold molecular nebula, as the displaced hot gas mass exceeds the cold gas mass, making uplift energetically feasible based on Archimedes’ principle. Further supporting this scenario is the alignment of the cold gas with the X-ray cavities and the bulk velocities of the H α filaments ($\sim 375 \text{ km s}^{-1}$), consistent with the terminal velocity of the rising bubbles.

However, the relatively low observed velocities of the cold gas, much lower than the ICM’s predicted turbulent velocity ($\sim 400 \text{ km s}^{-1}$; Sanders & Fabian 2013), may challenge the uplift hypothesis. The lower veloc-

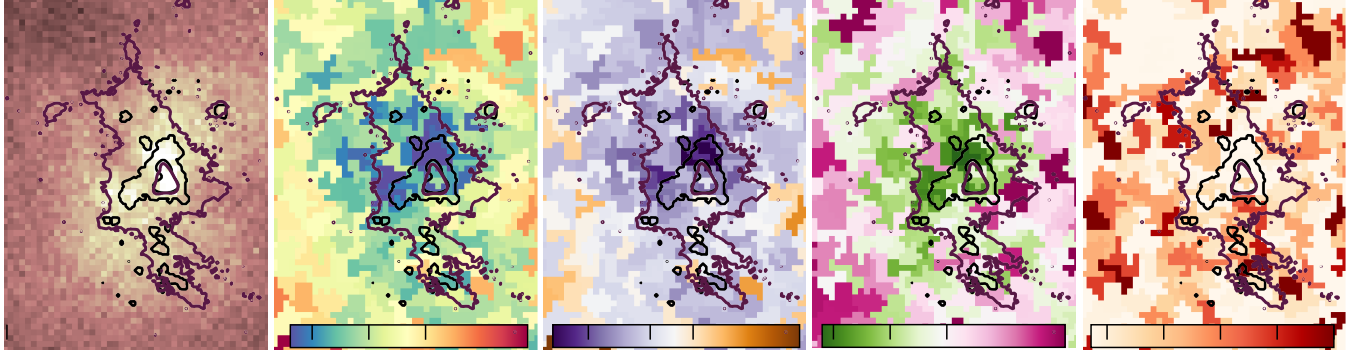


Figure 15. Spectral maps of the multiphase fountain in Abell 2597 with H α (purple contours) and CO(2-1) (black contours) overlaid. The maps highlight the relationship between X-ray-emitting hot gas and cooler phases. Cooler X-ray gas is cospatial with the multiphase filaments, reflecting ongoing radiative cooling, while localized regions of elevated temperature, entropy, and pressure are observed near the northern ghost cavities and along the filament bordering the southwestern ghost cavity. These regions are enriched in metals, consistent with AGN-driven outflows uplifting material and altering the thermodynamic state of the ICM.

ties of the cold gas suggest that it may have formed in situ through radiative cooling, consistent with hydrodynamical simulations that predict filament velocities dominated by bulk bubble motions rather than turbulence (e.g., Qiu et al. 2020; Zhang et al. 2022). Since the buoyant rise time of the bubbles ($\sim 10^8$ yr) is roughly consistent with the cooling time within the radius where cold filaments are observed, it is plausible that a fraction of the cold gas observed condensed from the warm gas while being uplifted.

Nonetheless, there is significant uncertainty in the ICM velocity dispersion measurement by Sanders & Fabian (2013). If the true velocity dispersion is closer to the 150 km s $^{-1}$ observed in Perseus (Hitomi Collaboration et al. 2016), then turbulence in the wake of the rising bubbles could still drive cold gas uplift. Future observations with XRISM will be critical in distinguishing between these scenarios, especially given that the kinematics of the extended multiphase nebula in Abell 2597 is mapped in incredible detail compared to other cool core clusters like Perseus and M87.

4.4.2. Spectral Properties

We present detailed spectral maps of the multiphase fountain in Figure 15, showing the relationship between the X-ray-emitting hot gas and the cooler phases traced by H α (purple contours) and CO(2-1) (black contours). As expected, the X-ray gas in regions cospatial with the multiphase filaments is very cool, reflecting the ongoing radiative cooling that occurs in these areas. However, localized regions of slightly higher temperatures are observed north of the H α filament near the northern ghost cavities and to the south along the filament bordering the southwestern ghost cavity.

The entropy and pressure maps also reveal a consistent pattern, with regions of elevated temperature also show-

ing slightly higher entropy and pressure—potentially reflecting AGN feedback altering the thermodynamic state of the uplifted gas. The abundance map further complements this picture, showing that areas of higher temperature, entropy, and pressure are also enriched in metals. These metal-rich regions likely result from AGN-driven winds transporting material outward from the core. For example, the enhanced abundance near the tip of the northern radio lobe suggests the lifting of metal-rich gas to larger radii, while elevated abundances along the rims of the teardrop cavity point to outward displacement of enriched material by the expanding cavity. Similarly, the abundance enhancement in the hot arc region appears linked to interactions between AGN-driven shocks and the surrounding gas, underscoring the lasting impact of past AGN activity on the ICM’s thermal and chemical properties.

5. THE ORIGIN OF THE X-RAY CHANNEL

The elongated X-ray surface brightness “channel” identified in Figure 1, running parallel to the northern radio jet axis, is likely a thin sheet of lower-density gas at the edge of the cluster’s cool core. Stretching approximately 60 kpc south of the southern radio jet and curving inward near the radio jet’s core to connect with the cluster center, this feature extends 57 kpc (37'') in length and is about 8 kpc (5'') wide. The temperature map in Figure ?? reveals that the gas along the channel is slightly hotter than the surrounding core, while the surface brightness profile (Figure 7) confirms an 11.6 σ drop within the channel region.

Similar channels have also been observed in other systems, such as the merging cluster Abell 520 and the sloshing cool core of Abell 2142 (Wang et al. 2016; Wang & Markevitch 2018). While such structures might theoretically result from two opposing cold fronts,

this scenario is unlikely for A2597, as it was for A520 and A2142. Instead, these features are more plausibly interpreted as plasma depletion layers (PDLs), a phenomenon observed near planets (e.g., Øieroset et al. 2004) and reproduced in magnetohydrodynamic (MHD) simulations of galaxy clusters (ZuHone 2011). PDLs form when magnetic field lines drape around a moving object—such as a galaxy, subcluster, or bubble—becoming stretched and more effective at scattering charged particles. This amplifies the magnetic field and reduces thermal pressure in the region, squeezing out plasma near the front when magnetic pressure reaches equipartition with the thermal pressure and creating a low-density channel.

In Abell 520, the observed PDL aligned with the direction of a secondary subcluster merger (Wang et al. 2016). However, Abell 2597 is a relaxed cluster with no evidence of a recent merger, making this explanation less likely. An alternative scenario involves the flow of magnetized plasma within a cool core. MHD simulations have shown that even tangled magnetic fields, typical of cluster environments, can drape and amplify near moving fronts, forming depletion layers (Dursi & Pfrommer 2008; ZuHone et al. 2014). The PDL in A2597 resembles the sheet-like features predicted in simulations of sloshing cores (e.g., Figure 23 of ZuHone et al. (2011)), where amplified magnetic fields align with, but are offset from, cold fronts. While the PDL in Abell 520 is observed near a cold front, A2597 does not exhibit obvious cold fronts unless we interpret the three shock fronts as such, particularly since the inner front is close to the PDL.

In the absence of a merger or cold front, strong velocity shear alone may be sufficient to amplify the magnetic field and create the observed channel. Preliminary results from Bellomi et al., in preparation, show that these regions form in somewhat random locations within the TNG Cluster simulations (Nelson et al. 2024; Truong et al. 2024). Regardless of its origin, the presence of this PDL indicates an amplified magnetic field within the cluster’s ICM, potentially shaped by AGN feedback or other dynamical processes. Further investigation with numerical simulations is needed to fully understand its formation and significance.

6. SUMMARY

In this paper, we presented deep (590 ks) *Chandra* X-ray observations of Abell 2597, complemented by archival GMRT radio data and SINFONI near-infrared observations, to study the interplay between AGN feedback, cooling, and supermassive black hole accretion in this canonical cool core galaxy cluster. The new X-ray data provide the most detailed view to date of Abell

2597’s ICM, revealing both new and previously identified X-ray cavities, potential shock fronts, and a distinct surface brightness channel. Together, these features offer fresh insights into AGN feeding and feedback processes in the cluster, while also confirming several long-standing hypotheses.

Our results are summarized as follows:

1. *Structures identified:* We identified two additional X-ray cavities, increasing the total to six in the cluster, along with three faint concentric rings in the outer ICM, which we interpret as potential shock fronts. Additionally, we identified an elongated X-ray surface brightness deficit, referred to as a “channel,” which we interpret as a plasma depletion layer.
2. *Duty Cycle of the AGN:* While it remains possible that the observed features result from a single active AGN cycle, the presence of potential shock fronts and the spectral index map lends support to the idea that the cavities were created over multiple cycles of AGN activity. We estimate a duty cycle of $\sim 10^7$ years, consistent with studies of other clusters exhibiting repeated rounds of AGN feedback.
3. *Inefficient Energy Injection from AGN Feedback:* The cavities and potential shock fronts inject energy into the ICM at an estimated rate of $\sim 10^{44}$ erg s $^{-1}$, comparable to the cluster’s cooling luminosity ($L_{\text{cool}} \sim 10^{44}$ erg s $^{-1}$). However, this energy appears insufficient to fully counteract radiative cooling. The residual X-ray and UV cooling rate is just enough to fill the $\sim 3.2 \times 10^9 M_\odot$ cold molecular gas reservoir near the cluster center, providing further evidence that AGN feedback alone does not entirely suppress cooling flows.
4. *Fueling the AGN:* We estimate a Bondi power of $P_{\text{Bondi}} \sim 2 \times 10^{43}$ erg s $^{-1}$, an order of magnitude lower than the cavity power, indicating that hot mode accretion alone cannot sustain the AGN. Archival ALMA observations of cold molecular clouds show motions consistent with infalling gas, supporting the chaotic cold accretion (CCA) scenario as the dominant fueling mechanism.
5. *The X-ray Channel:* The X-ray channel, spanning 57 kpc in length and 8 kpc in width, is oriented parallel to the northern radio jet. The feature is likely a plasma depletion layer formed by magnetic field amplification through strong velocity shear.

While our observations provide a detailed view of the interplay between AGN feedback and cooling in Abell 2597, several open questions concerning the precise mechanisms driving gas and metal uplift, the contributions of hot versus cold mode accretion, and the role of magnetic fields in shaping ICM structures require further exploration. Next-generation observatories, particularly with XRISM and high-resolution radio arrays, will be instrumental in addressing these uncertainties and advancing our understanding of feedback and accretion in cool-core clusters.

ACKNOWLEDGMENTS

The scientific results reported in this paper are based on observations from multiple ground- and space-based observatories, including the *Chandra* X-ray Observatory, the Giant Metrewave Radio Telescope (GMRT), the upgraded Giant Metrewave Radio Telescope (uGMRT), and the SINFONI near-infrared spectrograph on the Very Large Telescope (VLT).

Chandra data were obtained through programs supported by the Chandra X-ray Center (CXC), which is operated by the Smithsonian Astrophysical Observatory for NASA under contract NAS8-03060. The GMRT and uGMRT data were accessed through the National Centre for Radio Astrophysics (NCRA), Tata Institute of Fundamental Research (TIFR), located in Pune, India. GMRT is operated by NCRA-TIFR, and we acknowledge the significant contributions of its engineering and technical teams in making the observations possible. We also use SINFONI observations obtained at the Very Large Telescope (VLT) of the European Southern Observatory (ESO), Paranal, Chile, under program ID 0102.A-0463(A). These data were critical for mapping the distribution and kinematics of warm molecular gas in the cluster core. We acknowledge the efforts of the teams behind these facilities for enabling the collection of the high-quality data used in this work.

OO acknowledges support from the ALMA Student Observing Support grant. GRT acknowledges support for program HST-GO-16173.001-A, provided through a grant from the Space Telescope Science Institute under NASA contract NAS5-26555.

APPENDIX

A. DATA ANALYSIS

A.0.1. Imaging

We processed the X-ray observations using the MERGE_OBS script in CIAO. The highest resolution images presented maintain *Chandra*'s native resolution of $0''.5$, corresponding to a physical resolution of ~ 0.75 kpc. To enhance the visibility of sharp features and subtle structures in the intracluster gas, we created an unsharp-masked image by smoothing the data with a $0''.98$ Gaussian and subtracting it from the same image smoothed with a $9''.8$ Gaussian (e.g., [Hlavacek-Larrondo et al. 2012](#)). Additionally, we generated an adaptively smoothed image of the raw surface brightness map using a variable-width Gaussian kernel that adjusts its radius to match the local event density. All X-ray surface brightness contours displayed are derived from this adaptively smoothed image.

A.0.2. Spectral Analysis

We derived the spectral properties of A2597's ICM following the methodology detailed in [Vikhlinin et al. \(2006\)](#). For a comprehensive description of the entire procedure, we refer the reader to Section 2.3 of [Omoruyi et al. \(2023\)](#), where the same process was applied to SDSS 1531.

In brief, we extracted spectra from concentric annuli ($8''.5$ - $592''.8$, or 13-905 kpc) centered on the X-ray peak of the cleaned data from the central $8''.5$ to $r_{500} = 592''.8$, marked as the dashed white circle in the left panel of Figure 16. We also defined a $1''.0$ circle within the same chip but further from the cluster to encompass the local background and subtracted it from each annulus. We modeled the resulting profile with the modified β -model ([Cavaliere & Fusco-Femiano 1978; Vikhlinin et al. 2006](#)):

$$n_p n_e = n_0^2 \frac{(r/r_c)^{-\alpha}}{(1+r^2/r_c^2)^{3\beta-\alpha/2}} \frac{1}{(1+r^\gamma/r_s^\gamma)^{\epsilon/\gamma}} + \frac{n_{0,2}^2}{(1+r^2/r_c^2)^{3\beta_2}} \quad (\text{A1})$$

The best-fit model provided the three-dimensional gas density profile $\rho_g(r)$, from which we calculated the total gas mass M_g and estimated the classical cooling rate \dot{M}_{cool} .

We fit the temperature profile using 12 logarithmically-spaced annuli extending to $\sim 517''$, shown as the pink annuli in the left panel of Figure 16. After background subtraction, each annulus contained at least 74,000 net counts. We modeled the temperature using the three-dimensional analytic model (Vikhlinin et al. 2006):

$$T_{3D}(r) = T_0 \frac{x + T_{\min}/T_0}{x + 1} \frac{(r/r_t)^{-a}}{\left[1 + (r/r_t)^b\right]^{c/b}}, \quad (\text{A2})$$

and projected it to create the temperature profile.

Finally, we calculated the total cluster mass within radius r using the equation for hydrostatic equilibrium (Sarazin 1988), and the derived gas density and temperature profiles. We adopted M_{500} and R_{500} from the $Y_X - M$ scaling relation (Vikhlinin et al. 2009), as the hydrostatic mass estimate is most reliable in the central region. We denote masses from the scaling relation as $M_{500} - Y_X$ and those from hydrostatic equilibrium as M_{HE} .

To generate high-resolution temperature, pressure, and entropy maps, we used the Contour Binning algorithm described in Sanders (2006). The algorithm selects regions based on a minimum S/N threshold, growing bins along contours of surface brightness until the threshold is met. The algorithm identified 1449 spatial bins in an adaptively smoothed image ($S/N = 3$ in the 0.5–7 keV band) with a minimum $S/N = 30$, which led about 300 net counts per bin, while using a geometric constraint factor of $C = 2$ to ensure compact bin shapes. Point sources were masked out from the X-ray image prior to binning.

Subsequently, we used J. Sanders' ‘make_region_files’ code to create CIAO-compatible region files for each bin. We then extracted corresponding source and background spectra for each region in all event files for each ObsID, generating associated response files (ARF/RMF). The summed spectra were fit simultaneously in XSPEC using absorbed MEKAL models, with redshift, Galactic N_H , and metallicity fixed to $z = 0.0821$, $N_H = 2.252 \times 10^{20} \text{ cm}^{-2}$ ², and $Z = 0.3Z_\odot$, respectively.

From the best-fit parameters for the temperature kT and normalization per square arcsecond $N(r)$, we constructed projected maps of temperature, entropy, and pressure using J. Sanders' PAINT_OUTPUT_IMAGES. We derived the temperature and metallicity maps directly from the best-fit kT and abundance values. We created pseudo-entropy and pressure maps by assuming the electron density is proportional to the square root of the fitted normalization. Note that this assumption is inaccurate as it requires uncertain volume assumptions, hence the term ‘pseudo.’ From here, we create pseudo pressure (P) and entropy (S) maps using the equations $P \equiv 1.83n_e kT$, and $S \equiv kT n_e^{-2/3}$, giving units of keV $\text{cm}^{-5/2}$ arcsec^{-1} for the pressure and keV $\text{cm}^{5/3}$ $\text{arcsec}^{2/3}$ for the entropy.

We present and analyze the resulting X-ray deep image, spectral fits, profiles, and maps in Section ??.

B. SINFONI OBSERVATIONS

The SINFONI-AO data reduction was performed using ESOREX (3.13.6) following the workflow 3.3.2 under the EsoReflex environment (Freudling et al. 2013). The pipeline first corrected all target and sky exposures for darks, flats, geometrical distortions, and differential atmospheric refraction. Then, the sky background was subtracted by using the sky exposures, the wavelength calibration was performed through the observations of a Th-Ar reference arc lamp, and the data cubes were built for each exposure by combining the corrected target frames. We modeled the emission lines in the data cubes using the public Python spectroscopic analysis toolkit (PYSPECKIT, Ginsburg et al. (2022)). The package uses a Levenberg-Marquardt algorithm via the MPFIT (Markwardt 2009) and LMFIT (Newville et al. 2014) implementations. To fit the emission lines, we first subtracted the continuum emission stemming from the host stellar component in the nearby line-free regions for each emission line. We then fit the H₂ emission lines with Gaussian profiles, using a single narrow component for each line.

REFERENCES

Alexander, D. M., & Hickox, R. C. 2012, *\nar*, 56, 93,

² (estimated using NASA's HEASARC N_H Column Density tool,
Bekhti et al. 2016)

doi: 10.1016/j.newar.2011.11.003

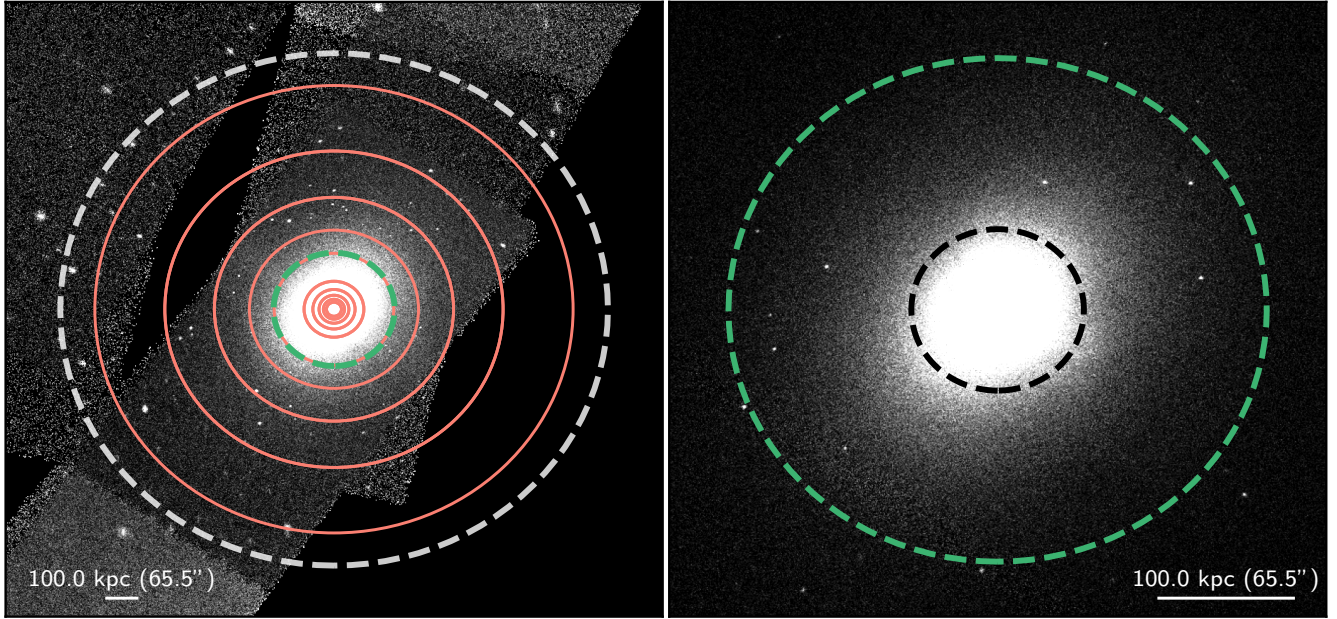


Figure 16. Exposure-corrected 0.7–2.0 keV *Chandra* X-ray maps of Abell 2597’s hot intracluster medium (ICM). The left panel shows the full extent of the ICM out to r_{500} (white dashed circle), with pink concentric rings indicating the annuli used to extract spectra for the thermodynamic profiles. The surface brightness profile is extracted from more finely spaced annuli within r_{500} . Although the majority of the emission is concentrated within the central 250 kpc of the cluster (green dashed circle), the outer annuli still contain at least 70,000 net counts. The right panel zooms into the central 250 kpc region, with the innermost 65 kpc highlighted by the innermost dashed black circle. These regions, where the ICM is densest and most of the physical features are observed, are the focus of the subsequent figures. All maps presented in this paper are centered at RA = 23h25m19.75s and Dec = $-12^{\circ}07'27''$ (J2000).

Allen, S. W., Dunn, R. J. H., Fabian, A. C., Taylor, G. B., & Reynolds, C. S. 2006, Monthly Notices of the Royal Astronomical Society, 372, 21, doi: [10.1111/j.1365-2966.2006.10778.x](https://doi.org/10.1111/j.1365-2966.2006.10778.x)

Bekhti, N. B., Flöer, L., Keller, R., et al. 2016, Astronomy & Astrophysics, 594, A116, doi: [10.1051/0004-6361/201629178](https://doi.org/10.1051/0004-6361/201629178)

Bonnet, H., Strobele, S., Biancat-Marchet, F., et al. 2003, in Adaptive Optical System Technologies II, Vol. 4839 (SPIE), 329–343, doi: [10.1117/12.457060](https://doi.org/10.1117/12.457060)

Bower, R. G., Benson, A. J., Malbon, R., et al. 2006, MNRAS, 370, 645, doi: [10.1111/j.1365-2966.2006.10519.x](https://doi.org/10.1111/j.1365-2966.2006.10519.x)

Bîrzan, L., Rafferty, D. A., McNamara, B. R., Wise, M. W., & Nulsen, P. E. J. 2004, The Astrophysical Journal, 607, 800, doi: [10.1086/383519](https://doi.org/10.1086/383519)

Cavaliere, A., & Fusco-Femiano, R. 1978, Astronomy and Astrophysics, 70, 677. <https://ui.adsabs.harvard.edu/abs/1978A&A....70..677C/abstract>

Churazov, E., Brüggen, M., Kaiser, C. R., Böhringer, H., & Forman, W. 2001, ApJ, 554, 261, doi: [10.1086/321357](https://doi.org/10.1086/321357)

Churazov, E., Sunyaev, R., Forman, W., & Böhringer, H. 2002, MNRAS, 332, 729, doi: [10.1046/j.1365-8711.2002.05332.x](https://doi.org/10.1046/j.1365-8711.2002.05332.x)

Clarke, T. E., Sarazin, C. L., Blanton, E. L., Neumann, D. M., & Kassim, N. E. 2005, The Astrophysical Journal, 625, 748, doi: [10.1086/429717](https://doi.org/10.1086/429717)

Croton, D. J., Springel, V., White, S. D. M., et al. 2006, Monthly Notices of the Royal Astronomical Society, 365, 11, doi: [10.1111/j.1365-2966.2005.09675.x](https://doi.org/10.1111/j.1365-2966.2005.09675.x)

Dursi, L. J., & Pfrommer, C. 2008, The Astrophysical Journal, 677, 993, doi: [10.1086/529371](https://doi.org/10.1086/529371)

Eisenhauer, F., Abuter, R., Bickert, K., et al. 2003, in Instrument Design and Performance for Optical/Infrared Ground-based Telescopes, Vol. 4841 (SPIE), 1548–1561, doi: [10.1117/12.459468](https://doi.org/10.1117/12.459468)

Fabian, A. C. 2012, Annual Review of Astronomy and Astrophysics, 50, 455, doi: [10.1146/annurev-astro-081811-125521](https://doi.org/10.1146/annurev-astro-081811-125521)

Fabian, A. C., Ferland, G. J., Sanders, J. S., et al. 2022a, Monthly Notices of the Royal Astronomical Society, 515, 3336, doi: [10.1093/mnras/stac2003](https://doi.org/10.1093/mnras/stac2003)

Fabian, A. C., Sanders, J. S., Allen, S. W., et al. 2003, Monthly Notices of the Royal Astronomical Society, 344, L43, doi: [10.1046/j.1365-8711.2003.06902.x](https://doi.org/10.1046/j.1365-8711.2003.06902.x)

Fabian, A. C., Sanders, J. S., Ferland, G. J., et al. 2023, Monthly Notices of the Royal Astronomical Society, 524, 716, doi: [10.1093/mnras/stad1870](https://doi.org/10.1093/mnras/stad1870)

- Fabian, A. C., Sanders, J. S., Taylor, G. B., et al. 2006, Monthly Notices of the Royal Astronomical Society, 366, 417, doi: [10.1111/j.1365-2966.2005.09896.x](https://doi.org/10.1111/j.1365-2966.2005.09896.x)
- Fabian, A. C., ZuHone, J. A., & Walker, S. A. 2022b, Monthly Notices of the Royal Astronomical Society, 510, 4000, doi: [10.1093/mnras/stab3655](https://doi.org/10.1093/mnras/stab3655)
- Freudling, W., Romaniello, M., Bramich, D. M., et al. 2013, Astronomy & Astrophysics, 559, A96, doi: [10.1051/0004-6361/201322494](https://doi.org/10.1051/0004-6361/201322494)
- Fruscione, A., McDowell, J. C., Allen, G. E., et al. 2006, in Observatory Operations: Strategies, Processes, and Systems, Vol. 6270 (SPIE), 586–597, doi: [10.1117/12.671760](https://doi.org/10.1117/12.671760)
- Gaspari, M., Ruszkowski, M., & Oh, S. P. 2013, Monthly Notices of the Royal Astronomical Society, 432, 3401, doi: [10.1093/mnras/stt692](https://doi.org/10.1093/mnras/stt692)
- Gaspari, M., Ruszkowski, M., & Sharma, P. 2012, The Astrophysical Journal, 746, 94, doi: [10.1088/0004-637X/746/1/94](https://doi.org/10.1088/0004-637X/746/1/94)
- Gaspari, M., Temi, P., & Brightenti, F. 2016, ArXiv e-prints
- Gaspari, M., McDonald, M., Hamer, S. L., et al. 2018, The Astrophysical Journal, 854, 167, doi: [10.3847/1538-4357/aaaa1b](https://doi.org/10.3847/1538-4357/aaaa1b)
- Ginsburg, A., Sokolov, V., Val-Borro, M. d., et al. 2022, The Astronomical Journal, 163, 291, doi: [10.3847/1538-3881/ac695a](https://doi.org/10.3847/1538-3881/ac695a)
- Hitomi Collaboration, Aharonian, F., Akamatsu, H., et al. 2016, *\nat*, 535, 117, doi: [10.1038/nature18627](https://doi.org/10.1038/nature18627)
- Hlavacek-Larrondo, J., Fabian, A. C., Edge, A. C., et al. 2012, Monthly Notices of the Royal Astronomical Society, 421, 1360, doi: [10.1111/j.1365-2966.2011.20405.x](https://doi.org/10.1111/j.1365-2966.2011.20405.x)
- Hlavacek-Larrondo, J., McDonald, M., Benson, B. A., et al. 2015, The Astrophysical Journal, 805, 35, doi: [10.1088/0004-637X/805/1/35](https://doi.org/10.1088/0004-637X/805/1/35)
- Kereš, D., Katz, N., Weinberg, D. H., & Davé, R. 2005, Monthly Notices of the Royal Astronomical Society, 363, 2, doi: [10.1111/j.1365-2966.2005.09451.x](https://doi.org/10.1111/j.1365-2966.2005.09451.x)
- Kirkpatrick, C. C., McNamara, B. R., Rafferty, D. A., et al. 2009, *\apj*, 697, 867, doi: [10.1088/0004-637X/697/1/867](https://doi.org/10.1088/0004-637X/697/1/867)
- Koekemoer, A. M., O’Dea, C. P., Sarazin, C. L., et al. 1999, *\apj*, 525, 621, doi: [10.1086/307911](https://doi.org/10.1086/307911)
- Kormendy, J., & Ho, L. C. 2013, *\araa*, 51, 511, doi: [10.1146/annurev-astro-082708-101811](https://doi.org/10.1146/annurev-astro-082708-101811)
- Landau, L. D., & Lifshitz, E. M. 1959, Fluid mechanics. <https://ui.adsabs.harvard.edu/abs/1959flme.book.....L>
- Liu, W., Sun, M., Nulsen, P., et al. 2019, Monthly Notices of the Royal Astronomical Society, 484, 3376, doi: [10.1093/mnras/stz229](https://doi.org/10.1093/mnras/stz229)
- Markevitch, M., & Vikhlinin, A. 2007, Physics Reports, 443, 1, doi: [10.1016/j.physrep.2007.01.001](https://doi.org/10.1016/j.physrep.2007.01.001)
- Markwardt, C. B. 2009, ASP. <https://articles.adsabs.harvard.edu/full/2009ASPC..411..251M>
- McConnell, N. J., Ma, C.-P., Gebhardt, K., et al. 2011, Nature, 480, 215, doi: [10.1038/nature10636](https://doi.org/10.1038/nature10636)
- McNamara, B., & Nulsen, P. 2007, Annual Review of Astronomy and Astrophysics, 45, 117, doi: [10.1146/annurev.astro.45.051806.110625](https://doi.org/10.1146/annurev.astro.45.051806.110625)
- McNamara, B. R., & Nulsen, P. E. J. 2012, New Journal of Physics, 14, 055023, doi: [10.1088/1367-2630/14/5/055023](https://doi.org/10.1088/1367-2630/14/5/055023)
- McNamara, B. R., Wise, M. W., Nulsen, P. E. J., et al. 2001, The Astrophysical Journal, 562, L149, doi: [10.1086/338326](https://doi.org/10.1086/338326)
- Nelson, D., Pillepich, A., Ayromlou, M., et al. 2024, Astronomy & Astrophysics, 686, A157, doi: [10.1051/0004-6361/202348608](https://doi.org/10.1051/0004-6361/202348608)
- Newville, M., Stensitzki, T., Allen, D. B., & Ingargiola, A. 2014, LMFIT: Non-Linear Least-Square Minimization and Curve-Fitting for Python, Zenodo, doi: [10.5281/zenodo.11813](https://doi.org/10.5281/zenodo.11813)
- Nulsen, P. E. J., McNamara, B. R., Wise, M. W., & David, L. P. 2005, The Astrophysical Journal, 628, 629, doi: [10.1086/430845](https://doi.org/10.1086/430845)
- Oegerle, W. R., Cowie, L., Davidsen, A., et al. 2001, The Astrophysical Journal, 560, 187, doi: [10.1086/322246](https://doi.org/10.1086/322246)
- Omoruyi, O., Tremblay, G. R., Combes, F., et al. 2023, “Beads on a String” Star Formation Tied to one of the most Powerful AGN Outbursts Observed in a Cool Core Galaxy Cluster, arXiv, doi: [10.48550/arXiv.2312.06762](https://doi.org/10.48550/arXiv.2312.06762)
- Oonk, J. B. R., Jaffe, W., Bremer, M. N., & van Weeren, R. J. 2010, Monthly Notices of the Royal Astronomical Society, 405, 898, doi: [10.1111/j.1365-2966.2010.16535.x](https://doi.org/10.1111/j.1365-2966.2010.16535.x)
- Pizzolato, F., & Soker, N. 2005, *\apj*, 632, 821, doi: [10.1086/444344](https://doi.org/10.1086/444344)
- Qiu, Y., Bogdanović, T., Li, Y., McDonald, M., & McNamara, B. R. 2020, Nature Astronomy, 4, 900, doi: [10.1038/s41550-020-1090-7](https://doi.org/10.1038/s41550-020-1090-7)
- Rafferty, D. A., McNamara, B. R., Nulsen, P. E. J., & Wise, M. W. 2006, The Astrophysical Journal, 652, 216, doi: [10.1086/507672](https://doi.org/10.1086/507672)
- Randall, S. W., Forman, W. R., Giacintucci, S., et al. 2010, The Astrophysical Journal, 726, 86, doi: [10.1088/0004-637X/726/2/86](https://doi.org/10.1088/0004-637X/726/2/86)
- Randall, S. W., Nulsen, P. E. J., Jones, C., et al. 2015, The Astrophysical Journal, 805, 112, doi: [10.1088/0004-637X/805/2/112](https://doi.org/10.1088/0004-637X/805/2/112)
- Russell, H. R., Fabian, A. C., McNamara, B. R., & Broderick, A. E. 2015, Monthly Notices of the Royal Astronomical Society, 451, 588, doi: [10.1093/mnras/stv954](https://doi.org/10.1093/mnras/stv954)

- Russell, H. R., Sanders, J. S., Fabian, A. C., et al. 2010, Monthly Notices of the Royal Astronomical Society, 406, 1721, doi: [10.1111/j.1365-2966.2010.16822.x](https://doi.org/10.1111/j.1365-2966.2010.16822.x)
- Russell, H. R., McNamara, B. R., Edge, A. C., et al. 2013, ArXiv e-prints
- Sanders, J. S. 2006, Monthly Notices of the Royal Astronomical Society, 371, 829, doi: [10.1111/j.1365-2966.2006.10716.x](https://doi.org/10.1111/j.1365-2966.2006.10716.x)
- Sanders, J. S., & Fabian, A. C. 2013, Monthly Notices of the Royal Astronomical Society, 429, 2727, doi: [10.1093/mnras/sts543](https://doi.org/10.1093/mnras/sts543)
- Sarazin, C. 1988, X-ray Emission from Clusters of Galaxies. <http://ned.ipac.caltech.edu/level5/March02/Sarazin/frames.html>
- Sarazin, C. L., Finoguenov, A., Wik, D. R., & Clarke, T. E. 2016, Deep XMM-Newton Observations of the NW Radio Relic Region of Abell 3667, doi: [10.48550/arXiv.1606.07433](https://doi.org/10.48550/arXiv.1606.07433)
- Simionescu, A., Werner, N., Böhringer, H., et al. 2009, Astronomy & Astrophysics, 493, 409, doi: [10.1051/0004-6361:200810225](https://doi.org/10.1051/0004-6361:200810225)
- Snios, B., Nulsen, P. E. J., Wise, M. W., et al. 2018, The Astrophysical Journal, 855, 71, doi: [10.3847/1538-4357/aaaf1a](https://doi.org/10.3847/1538-4357/aaaf1a)
- Tremblay, G. R., O'Dea, C. P., Baum, S. A., et al. 2012a, Monthly Notices of the Royal Astronomical Society, 424, 1026, doi: [10.1111/j.1365-2966.2012.21281.x](https://doi.org/10.1111/j.1365-2966.2012.21281.x)
- Tremblay, G. R., O'Dea, C. P., Baum, S. A., et al. 2012b, Monthly Notices of the Royal Astronomical Society, 424, 1042, doi: [10.1111/j.1365-2966.2012.21278.x](https://doi.org/10.1111/j.1365-2966.2012.21278.x)
- Tremblay, G. R., Oonk, J. B. R., Combes, F., et al. 2016, Nature, 534, 218, doi: [10.1038/nature17969](https://doi.org/10.1038/nature17969)
- Tremblay, G. R., Combes, F., Oonk, J. B. R., et al. 2018, The Astrophysical Journal, 865, 13, doi: [10.3847/1538-4357/aad6dd](https://doi.org/10.3847/1538-4357/aad6dd)
- Truong, N., Pillepich, A., Nelson, D., et al. 2024, Astronomy & Astrophysics, 686, A200, doi: [10.1051/0004-6361/202348562](https://doi.org/10.1051/0004-6361/202348562)
- Ubertosi, F., Gitti, M., Brightenti, F., et al. 2023, The Astrophysical Journal, 944, 216, doi: [10.3847/1538-4357/acacf9](https://doi.org/10.3847/1538-4357/acacf9)
- Vantyghem, A. N., McNamara, B. R., Russell, H. R., et al. 2014, Monthly Notices of the Royal Astronomical Society, 442, 3192, doi: [10.1093/mnras/stu1030](https://doi.org/10.1093/mnras/stu1030)
- Veilleux, S., Cecil, G., & Bland-Hawthorn, J. 2005, *\araa*, 43, 769, doi: [10.1146/annurev.astro.43.072103.150610](https://doi.org/10.1146/annurev.astro.43.072103.150610)
- Vikhlinin, A., Burenin, R., Forman, W. R., et al. 2007, in Heating versus Cooling in Galaxies and Clusters of Galaxies, ed. H. Böhringer, G. Pratt, A. Finoguenov, & P. Schuecker, Eso Astrophysics Symposia (Berlin, Heidelberg: Springer), 48–53, doi: [10.1007/978-3-540-73484-0_9](https://doi.org/10.1007/978-3-540-73484-0_9)
- Vikhlinin, A., Kravtsov, A., Forman, W., et al. 2006, The Astrophysical Journal, 640, 691, doi: [10.1086/500288](https://doi.org/10.1086/500288)
- Vikhlinin, A., McNamara, B. R., Forman, W., et al. 1998, The Astrophysical Journal, 502, 558, doi: [10.1086/305951](https://doi.org/10.1086/305951)
- Vikhlinin, A., Burenin, R. A., Ebeling, H., et al. 2009, The Astrophysical Journal, 692, 1033, doi: [10.1088/0004-637X/692/2/1033](https://doi.org/10.1088/0004-637X/692/2/1033)
- Voit, G. M., Meece, G., Li, Y., et al. 2017, The Astrophysical Journal, 845, 80, doi: [10.3847/1538-4357/aa7d04](https://doi.org/10.3847/1538-4357/aa7d04)
- Wang, Q. H. S., & Markevitch, M. 2018, The Astrophysical Journal, 868, 45, doi: [10.3847/1538-4357/aae921](https://doi.org/10.3847/1538-4357/aae921)
- Wang, Q. H. S., Markevitch, M., & Giacintucci, S. 2016, The Astrophysical Journal, 833, 99, doi: [10.3847/1538-4357/833/1/99](https://doi.org/10.3847/1538-4357/833/1/99)
- Zhang, C., Zhuravleva, I., Gendron-Marsolais, M.-L., et al. 2022, Monthly Notices of the Royal Astronomical Society, 517, 616, doi: [10.1093/mnras/stac2282](https://doi.org/10.1093/mnras/stac2282)
- ZuHone, J. A. 2011, The Astrophysical Journal, 728, 54, doi: [10.1088/0004-637X/728/1/54](https://doi.org/10.1088/0004-637X/728/1/54)
- ZuHone, J. A., Kunz, M. W., Markevitch, M., Stone, J. M., & Biffi, V. 2014, The Astrophysical Journal, 798, 90, doi: [10.1088/0004-637X/798/2/90](https://doi.org/10.1088/0004-637X/798/2/90)
- ZuHone, J. A., Markevitch, M., & Lee, D. 2011, The Astrophysical Journal, 743, 16, doi: [10.1088/0004-637X/743/1/16](https://doi.org/10.1088/0004-637X/743/1/16)
- Øieroset, M., Mitchell, D. L., Phan, T. D., et al. 2004, Space Science Reviews, 111, 185, doi: [10.1023/B:SPAC.0000032715.69695.9c](https://doi.org/10.1023/B:SPAC.0000032715.69695.9c)